

# The asymmetric structure of the inner disc around HD 142527 A with VLTI/MATISSE

M. B. Scheuck<sup>1,2</sup>, R. van Boekel<sup>1</sup>, Th. Henning<sup>1</sup>, P. A. Boley<sup>1</sup>, J. Varga<sup>3</sup>, A. Matter<sup>4</sup>, A. Penzlin<sup>5</sup>, J. H. Leftley<sup>4</sup>, L. van Haastere<sup>6</sup>, K. Perraut<sup>7</sup>, L. Labadie<sup>8</sup>, M. Min<sup>9,10</sup>, J. P. Berger<sup>7</sup>, L. B. F. M. Waters<sup>10,11</sup>, S. Zieba<sup>12</sup>, B. Lopez<sup>4</sup>, F. Lykou<sup>3</sup>, J.-C. Augereau<sup>7</sup>, P. Cruzalèbes<sup>4</sup>, W. C. Danchi<sup>13</sup>, V. Gámez Rosas<sup>14</sup>, M. Hogerheijde<sup>6</sup>, M. Letessier<sup>7</sup>, J. Scigliuto<sup>4</sup>, G. Weigelt<sup>15</sup>, S. Wolf<sup>16</sup>, and the MATISSE and GRAVITY collaborations

<sup>1</sup> Max-Planck-Institut für Astronomie, Königstuhl 17, 69117 Heidelberg, Germany  
 e-mail: scheuck@mpia.de

<sup>2</sup> Fakultät für Physik und Astronomie, Universität Heidelberg, Im Neuenheimer Feld 226, 69120 Heidelberg, Germany

<sup>3</sup> HUN-REN Research Centre for Astronomy and Earth Sciences, Konkoly Observatory, MTA Centre of Excellence, KonkolyThege Miklós út 15-17., H-1121 Budapest, Hungary

<sup>4</sup> Laboratoire Lagrange, Université Côte d'Azur, Observatoire de la Côte d'Azur, CNRS, Boulevard de l'Observatoire, CS 34229, 06304, Nice Cedex 4, France

<sup>5</sup> Ludwig-Maximilians-Universität München, Universitäts-Sternwarte, Scheinerstr. 1, 81679 München, Germany

<sup>6</sup> Leiden Observatory, Leiden University, PO Box 9513, 2300 RA, Leiden, The Netherlands

<sup>7</sup> Univ. Grenoble Alpes, CNRS, IPAG, 38000 Grenoble, France

<sup>8</sup> I. Physikalisches Institut, Universität zu Köln, Zülpicher Str. 77, 50937 Köln, Germany

<sup>9</sup> Anton Pannekoek Institute for Astronomy, University of Amsterdam, Science Park 904, 1098XH Amsterdam, The Netherlands

<sup>10</sup> SRON Netherlands Institute for Space Research, Niels Bohrweg 4, 2333 CA Leiden, The Netherlands

<sup>11</sup> Institute for Mathematics, Astrophysics and Particle Physics, Radboud University, P.O. Box 9010, MC 62 NL-6500 GL Nijmegen, The Netherlands

<sup>12</sup> Center for Astrophysics Harvard & Smithsonian: 60 Garden Street, Cambridge, MA 02138, USA

<sup>13</sup> NASA Goddard Space Flight Center, Astrophysics Division, Greenbelt, MD, 20771, USA

<sup>14</sup> STAR Institute, University of Liège, Quartier Agora - Bât. B5c Allée du Six Août 19C, B-4000 Liège, Belgium

<sup>15</sup> Max-Planck-Institut für Radioastronomie, Auf dem Hügel 69, 53121, Bonn, Germany

<sup>16</sup> Institute of Theoretical Physics and Astrophysics, University of Kiel, Leibnizstraße 15, 24118, Kiel, Germany

Accepted on February 2, 2026

## ABSTRACT

**Context.** Circumstellar discs, and especially their inner regions, covering ranges from  $<1$  au to a few astronomical units, are the birthplaces of terrestrial planets. The inner regions are thought to be similarly diverse in structure as the well-observed outer regions probed by ALMA.

**Aims.** Combining data and results from previous studies of the VLTI/PIONIER and VLTI/GRAVITY instruments with new, multi-epoch VLTI/MATISSE observations, we aim to provide a comprehensive picture of the structure of the inner regions of the circumstellar disc around the F-type Herbig Ae/Be star HD 142527 A, the primary of a binary star system.

**Methods.** We model the multi-wavelength interferometric data using a parametrised, geometrically thin disc model, allowing for azimuthal asymmetry, exploring a first-order disc modulation and an off-centre Gaussian component.

**Results.** We find time-variable structures in the  $N$ -band observables, which we reproduce with time-dependent models. This variability manifests as azimuthally asymmetric emission, evidenced by strong, non-zero closure phases in the  $N$ -band data. Fits to individual epochs of the  $N$ -band observations yield better  $\chi^2_r$  values than fits to all epochs simultaneously. This suggests substantial changes in the geometry of the inner disc emission from  $\sim 1$  au up to a few astronomical-unit scales from one year to the next. Moreover, our models produce a very close-in inner disc rim  $R_{\text{rim}} \approx 0.1$  au. All together, we find a very complex, substantially non-point symmetric and temporally-variable disc ( $r_{\text{out}} \lesssim 6$  au) around the primary.

**Conclusions.** The very close-in inner rim indicates the presence of material inside the typical wall-like sublimation radius  $R_{\text{rim,literature}} \approx 0.3$  au. The complex, temporally variable inner-disc geometry is likely affected or even caused by the close passing ( $\sim 5$  au) and short orbit ( $P \approx 24$  yr) of the companion HD 142527 B.

**Key words.** infrared: stars – protoplanetary disks – stars: individual: HD 142527 – stars: pre-main sequence – techniques: interferometric – techniques: spectroscopic

## 1. Introduction

Herbig Ae/Be and T Tauri stars are often accompanied by planet-forming discs composed of gas and dust within the first 10 Myr of their existence. These discs are highly complex environments, with properties such as their mass and chemical composition, in-

fluenced not only by the host star but also by various concurrent processes. Among these are: turbulence, winds, the growth and migration of dust grains, and stellar accretion (Andrews et al. 2018; Andrews 2020; Benisty et al. 2023; Birnstiel 2024). Observations at millimetre wavelengths and scattered-light im-

ages at optical and near-infrared (IR) wavelengths have mapped the outer regions of these discs (Pohl et al. 2017; Garufi et al. 2017, 2018), revealing diverse structures like zones, radial gaps, spiral arms, dust clumps, and other azimuthal asymmetries (ALMA Partnership et al. 2015; Rubinstein et al. 2018). These regions also serve as a rich reservoir of gas and dust essential for planetary system formation, as supported by numerous studies examining various disc systems (e.g. Boccaletti et al. 2020). Recent research has also provided more approaches on how to identify planets embedded within these discs (Fedele et al. 2017; Teague et al. 2018; Pinte et al. 2019), and in the case of PDS 70, at least two planets have been detected (Müller et al. 2018; Keppler et al. 2018; Haffert et al. 2019).

Similarly, the inner regions are likely to host smaller-scale structures akin to those observed in the outer disc (e.g. Menu et al. 2015; Varga et al. 2018; GRAVITY Collaboration et al. 2021; Kluska et al. 2022; Varga et al. 2024; GRAVITY Collaboration et al. 2024). Emerging evidence suggests that some of these substructures, such as radial gaps, are formed by young, accreting planets (Haffert et al. 2019; Pinte et al. 2019).

We aim to expand the knowledge of planet formation within circumstellar discs, and to complement previous and concurrent research by studying the innermost regions of the discs (from  $<1$  au scales up to a few astronomical units). Thus, we observe the mid-IR wavelength region with the spectro-interferometric multi aperture mid-IR spectroscopic experiment (MATISSE) instrument (Lopez et al. 2022) located at the very large telescopic interferometer (VLTI) on Cerro Paranal in Chile; operated by the European southern observatory (ESO). The MATISSE instrument at the VLTI offers spatial resolutions superior to those of single telescopes (e.g. the James Webb space telescope) as well as a broad wavelength range. These resolutions facilitate the study of the structure of the innermost disc regions.

In this work, our focus lies on HD 142527, a binary system comprised of an F-type Herbig Ae/Be star (Hunziker et al. 2021) accompanied by an M-dwarf companion (Biller et al. 2012; Lacour et al. 2016; Christiaens et al. 2018) on an eccentric orbit ( $e \approx 0.45-0.7$ , Claudi et al. 2019). HD 142527 A posses a circumstellar disc, which was determined to be close to face-on by observations with the VLTI/precision integrated-optics near-infrared imaging experiment (PIONIER) (Lazareff et al. 2017) and VLTI/GRAVITY (GRAVITY Collaboration et al. 2019) instruments, and the Atacama Large millimeter/submillimeter array (ALMA) (Casassus et al. 2013). These observations showed inclination angles of  $i_{\text{in}} \approx 20-33^\circ$  and position angles of  $\theta_{\text{in}} \approx 5-20^\circ$  (east of north). For the inner disc, fits to the  $N$ -band emission indicate a radial gap within this region, not resolved by either the spectro-polarimetric high-contrast exoplanet research (SPHERE) instrument or ALMA (Menu et al. 2015; Varga et al. 2018). The companion, HD 142527 B, is close to the inner disc (periapsis to apoapsis  $\sim 5-15$  au) and orbits within a large gap in the surrounding circumbinary disc ( $\sim 113-170$  au east to west edge) (Boehler et al. 2017). A possible explanation for the large gap between inner and outer disc could be one or multiple unseen planets (Lacour et al. 2016). From shadows cast from the inner onto the outer disc Marino et al. (2015) determined the misalignment ( $\Delta\theta_{\text{in-out}} = 70^\circ$ ) and the position angle of the inner disc ( $\theta_{\text{in}} = (352 \pm 5)^\circ$ ). The inclination and position angle of the outer disc were estimated to be  $i_{\text{out}} = 38^\circ 21$  and  $\theta_{\text{out}} = 162^\circ 72$  from ALMA observations (Bohn et al. 2022). These, as well as information on the stellar parameters of HD 142527 A & B plus the parameters of the orbit of the

companion and the outer disc can be found in Table 1.

In this work, we show the results of the observations of HD 142527 taken with MATISSE, together with combined modelling of previous observations from PIONIER and GRAVITY obtained by Lazareff et al. (2017) and GRAVITY Collaboration et al. (2019), respectively. Similar to earlier studies of young stellar objects (YSOs) (e.g. GRAVITY Collaboration et al. 2021; Varga et al. 2024), we focus on analysing these data by applying geometric disc models to determine the structure of the inner-disc region. In contrast to these earlier works, the plethora of observations from the  $H$  to, especially, the  $N$  band provides us with the opportunity to also study the time variability of HD 142527 over different epochs.

The paper is structured as follows: in Sect. 2 we give an overview of the MATISSE observations and provide the necessary background on data reduction and quality assessment. First results, directly obtained from the observations, are presented in Sect. 3. Our modelling approach is explained in Sect. 4, and discussed in Sect. 5, where the findings are placed into a wider context. Finally, we give a summary and conclusions in Sect. 6.

## 2. Observations

First, we provide a brief overview of the observations used, as well as the data treatment. Our work centres around eight observations of HD 142527 on the MATISSE instrument taken from 2021 to 2023, presented in Table A.1. These observations were obtained as part of the guaranteed time observation (GTO) survey ‘Initial conditions of planet formation in protoplanetary discs with GRA4MAT and MATISSE’. We excluded any observation with a coherence time  $\tau_0 < 2$  ms, seeing  $> 1.5''$  or obvious artefacts (such as glitches during the observations).

Each MATISSE data set covers a wide wavelength range from the  $L/M$  ( $2.8-4.2 \mu\text{m}/4.5-5 \mu\text{m}$ ) to the  $N$  band ( $8-13 \mu\text{m}$ ). Three of the eight data sets were obtained in the quadruplet using the 8.2 m unit telescopes (UTs). The rest were obtained with the 1.8 m auxilliary telescope (AT) small, medium, large, or extended configurations. With the associated baseline lengths  $B \approx 10-130$  m, we reach spatial resolutions of  $\theta = \frac{\lambda}{2B} \approx 30.9-2.4$  mas at  $3 \mu\text{m}$  and  $\theta \approx 123.8-9.5$  mas at  $12 \mu\text{m}$ . We are able to combine the AT with the UT observations for HD 142527, as the inner disc is fully contained within the field of view (FOV) for all configurations, while the outer disc lies outside of it, with any scattered light from it, most likely, resolved out. For the  $N$  band, we only make use of UT observations as the ATs have a poor signal-to-noise ratio (S/N).

The bulk of the MATISSE data were reduced using a modification<sup>1</sup> to the 2.0.2 version of the MATISSE data reduction software (DRS)<sup>2</sup> (Millour et al. 2016) in combination with the MATISSE tools<sup>3</sup>. This modified version implements an improved coherent processing, which now utilises the 2D Fourier transform of the interferograms (previously a 1D Fourier transform was used), which provides more accurate estimates of the correlated flux and differential phase. To calibrate this data, a bright and unresolved star with well-known properties (e.g. the limb darkened diameter (LDD)) and an airmass matching that of

<sup>1</sup>Expected to be included in the official 2.3.0 release by ESO.

<sup>2</sup>Provided by ESO at

<https://www.eso.org/sci/software/pipelines/matisse>.

<sup>3</sup>Additional tools for data reduction are available at the MATISSE GitHub organisation:

<https://github.com/Matisse-Consortium/tools>.

Table 1: Stellar parameters of HD 142527 A &amp; B, with outer disc and orbital parameters of the companion.

Parameter	Unit	Value	Reference
<b>HD 142527</b>			
RA (J2016)	(h:':")	15:56:41.87	(1)
DEC (J2016)	(°:':")	-42:19:23.67	(1)
$d$	(pc)	159.3 $\pm$ 0.7	(1)
<b>HD 142527 A</b>			
Spectral Type		F2–F3	(2 <sup>a</sup> )
$T_\star$	(K)	6500 $\pm$ 250	(2 <sup>a</sup> , 3, 4)
$M_\star$	( $M_\odot$ )	2.20 $\pm$ 0.05	(2 <sup>a</sup> )
$\log(L_\star/L_\odot)$		1.35 $\pm$ 0.01	(2 <sup>a</sup> )
$R_\star$	( $R_\odot$ )	3.46 $\pm$ 0.13	(2 <sup>a</sup> )
$t_\star$	(Myr)	4.40 <sup>+0.49</sup> <sub>-0.38</sub>	(2 <sup>a</sup> )
<b>HD 142527 B</b>			
<b>STAR</b>			
Spectral Type		M2.5 $\pm$ 0.1	(5)
$T_\star$	(K)	3500 $\pm$ 100	(5)
$M_\star$	( $M_\odot$ )	0.34 $\pm$ 0.06	(5)
$\log(L_\star/L_\odot)$		-0.60 $\pm$ 0.08	(5 <sup>b</sup> )
$R_\star$	( $R_\odot$ )	1.37 $\pm$ 0.05	(5)
$t_\star$	(Myr)	1.8 <sup>+1.2</sup> <sub>-0.5</sub>	(5)
<b>ORBIT</b>			
$a$	(mas)	67.80 $\pm$ 1.38	(6 <sup>c</sup> )
$e$		0.47 $\pm$ 0.01	(6)
$i$	(°)	149.47 $\pm$ 0.71	(6)
$\omega$	(°)	186.45 $\pm$ 0.48	(6)
$\Omega$	(°)	161.51 $\pm$ 1.01	(6)
$\tau$	(yr)	2020.42 $\pm$ 0.05	(6)
$P$	(yr)	23.50 $\pm$ 0.85	(6)
<b>Outer disc</b>			
$R_{\text{in, east}}$	(mas)	$\sim$ 714.29	(7 <sup>d</sup> )
$R_{\text{in, west}}$	(mas)	$\sim$ 1071.43	(7 <sup>d</sup> )
$R_{\text{out}}$	(mas)	$\sim$ 3500	(7 <sup>d</sup> )
$\Delta\theta_{\text{in-out}}$	(°)	70	(8)
$i_{\text{out}}$	(°)	38.21	(9)
$\theta_{\text{out}}$	(°)	162.72	(9)

**References.** (1) [Gaia Collaboration et al. \(2023\)](#); (2) [Guzmán-Díaz et al. \(2021\)](#); (3) [Fairlamb et al. \(2015\)](#); (4) [Vioque et al. \(2018\)](#); (5) [Christiaens et al. \(2018\)](#); (6) [Nowak et al. \(2024\)](#); (7) [Fukagawa et al. \(2006\)](#); (8) [Marino et al. \(2015\)](#); (9) [Bohn et al. \(2022\)](#);

**Notes.** <sup>(a, c, d)</sup> Converted to milliarsecond with GAIA EDR3  $d = 158.51$  pc ([Gaia Collaboration et al. 2021](#)), GAIA DR3, and GAIA DR2  $d \approx 140$  pc distance ([Gaia Collaboration et al. 2018](#)).  
<sup>(b)</sup> Computed with  $L = 4\pi R_\star^2 \sigma T_\star^4$  ([Dullemond & Monnier 2010](#)).

HD 142527 is observed close in time to it. A detailed description of the calibration process can be found in [Varga et al. \(2021\)](#).

From a standard reduction of a MATISSE observation, we obtain a total spectrum  $F_\nu$  (averaged from the four individual

VLTI telescopes), six correlated fluxes  $F_{\nu, \text{corr}}$ , and four closure phases  $\Phi_{\nu, \text{cp}}$ . The single-dish spectra are produced from the incoherently reduced and chopped data, whereas the correlated fluxes and the closure phases stem from the coherently reduced, non-chopped data. Detailed descriptions of a typical MATISSE observation and the data reduction can be found in the works by [Lopez et al. \(2022\)](#) and [Varga et al. \(2021, 2024\)](#). In the present work, we provide a brief overview of the differences between the chopped and non-chopped observing modes, as well as the incoherent and coherent reduction methods. When chopping is active, the pointing of the telescopes intermittently switches from the object to the sky background. This improves the S/N of the total spectrum by enabling background subtraction, but interferes with the stability of the (interferometric) fringe tracking ([Woillez et al. 2024](#)). Thereby worsening the quality of the correlated flux and differential phase measurements. Thus, the non-chopping mode is used for those quantities. In this mode, for the interferometric observables, the background is removed via optical path difference (OPD) modulation. During reduction, in the coherent mode, the individual frames of the observation are aligned, preserving the phase information ([Lopez et al. 2022](#)). The noisy correlated flux estimator is then computed over the entire exposure, from which the correlated flux and the differential phase can be extracted. In the incoherent mode, on the other hand, the measured intensities are averaged without preserving the phase information of the individual frames ([Petrov et al. 2020](#)). All the observations in this work were either observed in low spectral resolution or were observed in medium/high resolution and then rebinned to low spectral resolution during reduction/post-processing. This gives us data with a spectral resolution of  $R = \frac{\lambda}{\Delta\lambda} \approx 34$  in the  $L/M$  and  $R \approx 30$  in the  $N$  band.

In addition to the MATISSE data, we made use of archival  $H$  band (1.5–1.85  $\mu\text{m}$ ) observations from the optical interferometry database (OiDB) at the Jean-Marie Mariotti centre (JMMC), taken with the PIONIER instrument ([Lazareff et al. 2017](#)). Moreover,  $K$  band (1.95–2.45  $\mu\text{m}$ ) observations provided by the GRAVITY collaboration, taken by the second-generation VLTI instrument of the same name ([GRAVITY Collaboration et al. 2017](#)).

### 3. Results

Before the modelling, we give a first interpretation of the calibrated data from the Figs. presented in Appendix A. Within the  $H$ ,  $K$ ,  $L$ , and  $N$  band, the correlated fluxes reach values of 3.46, 3.02, 2.03 and 0.63 Jy, for the longest baselines of 139.93, 129.23, 130.19, and 130.19 m, over all observations. For the same body of observations and baselines, the closure phases reach values of 2°67, 2°52, 10°97 and 47°20.

We are particularly interested in the  $N$ -band data of HD 142527 as it allows us to probe the disc up to a few astronomical units. The correlated fluxes reveal contributions from spatially unresolved disc regions. At first order, the longer the baseline (i.e. the higher the spatial frequency), the closer (to the centre) and smaller the disc region probed ([Buscher & Longair 2015](#)). The lower spatial frequencies of the  $N$  band, coupled with its sensitivity to cooler dust, make it a good indicator for the structure and composition of the extended inner disc regions (up to  $\sim 10$  au). Moreover, HD 142527 shows strong silicate features in both total spectra and correlated fluxes (Fig. A.1). In particular, for the  $N$  band, we see the silicate features disappear for several spatial frequencies (Figs. A.4 and A.5). This could be an indicator of a multiple-zone structure that cancels out the silicate emission (e.g. [Varga et al. 2024](#)). The prominence of the silicate

feature lines up with previous observations by [van Boekel et al. \(2005\)](#) and [Juhász et al. \(2010\)](#). The total spectra of the three epochs show a very similar shape with several crystalline silicate peaks, notably, the  $11.3\text{ }\mu\text{m}$  forsterite peak. Moreover, we find a  $\sim 10\%$  flux level variability across the epochs. Such a variation stays within the flux calibration uncertainties and is consistent with archival  $N$ -band data obtained with wide-field infrared survey explorer (WISE), infrared space observatory (ISO)/short wavelength spectrometer (SWS), and SPITZER (SPITZER). The other  $N$ -band observable is the closure phase  $\Phi_{\nu,\text{cp}}$ , which traces brightness asymmetries. HD 142527 shows large closure phases between the different epochs, suggesting a complex structure.

On the other hand, the shorter wavelength bands ( $H$ ,  $K$ ,  $L$ , and  $M$ ) resolve compact structure close to the star (sub- $\text{au}$ ), due to the higher spatial frequencies from the AT observation. This wavelength range shows a less pronounced signal for the closure phase, which increases from  $H$  to  $M$  band.

Comparing the  $N$ -band observations to the shorter wavelengths, we see that HD 142527 is already quite resolved (i.e. the correlated fluxes are closer to zero), while the opposite is true for the shorter wavelengths. This is, in part, due to the star contributing more at the shorter wavelengths, causing higher correlated fluxes. Moreover, we observe a first zero-crossing of the complex correlated fluxes at spatial frequencies  $\sim 15\text{ M}\lambda$ , with the next zero-crossing presumably occurring at spatial frequencies outside of our coverage ( $\sim 120 - 150\text{ M}\lambda$ ). The spatial frequency of zero-crossings is a particularly robust feature of our data, as it is not affected by calibration uncertainties. Furthermore, an increase in the closure phase from  $H$  to  $N$  band is apparent. This indicates a relatively symmetric structure on the smallest scales we resolve, whereas the larger scales of  $\sim 1\text{ au}$  show stronger asymmetry, which may be indicative of a two-component structure with an asymmetric, extended component seen at longer wavelengths, in addition to a more compact, relatively symmetric component seen at shorter wavelengths. We explore this in more detail via geometric modelling in Sects. 4.3 and 5.

## 4. Modelling

We model our data using a geometrically thin disc model, first without and then with azimuthal asymmetries. The opacity of the disc material is obtained from a fit to the total intensity spectrum in the  $N$  band (Sect. 4.1), showing a silicate emission feature with strong signs of high-temperature dust processing (e.g. [Bouwman et al. 2001](#); [van Boekel et al. 2004, 2005](#); [Juhász et al. 2010](#)). From this fit, we derive a ‘silicate’ and ‘continuum’ opacity component that we use in the interferometric modelling, allowing their relative ratio to vary in the different disc zones (Section 4.2.2).

As we lack a sufficient sampling of spatial frequencies ( $u, v$ ) needed for image reconstruction, we applied a parametric modelling approach. Fitting our model  $M$  to data  $D$  was done with Bayesian inference, implemented via the `dynesty`<sup>4</sup> package ([Speagle 2020](#)). The stopping criterion for this algorithm is the difference  $\Delta \ln \mathcal{Z}_i$  between the current estimated  $\mathcal{Z}_i$  and remaining evidence  $\Delta \mathcal{Z}_i$  at each iteration  $i$ . We chose  $\Delta \ln \mathcal{Z}_i < 0.01$ , which should be sufficient so that convergence is reached when the sampler terminates. For all parameters flat priors  $\pi(\Theta) \equiv P(\Theta, M)$  were employed. The amount of live points  $K_i$  (i.e. sam-

<sup>4</sup>A nested sampling algorithm based on Bayesian inference available at <https://zenodo.org/records/12537467>.

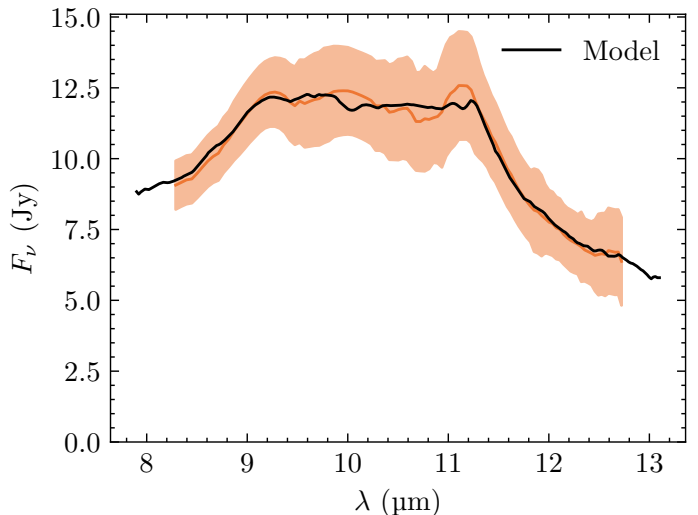


Fig. 1: Opacity fit. The model (black) is overlaid onto the averaged  $N$ -band UT data (orange). Here, the PAH flux contribution is excluded from the model curve as is the case for the disc modelling in Sect. 4.2.

ples drawn from the prior volume  $X$ ) was set to be 1000. The value of all parameters  $\Theta$  are the median of all samples, while the lower and upper uncertainty are the samples at 2.5 % and 97.5 %, respectively. More details on the fitting algorithm are provided in Appendix B. Additionally, an overview of all model parameters is provided in Table C.1.

We de-reddened the data, assuming foreground extinction (see Appendix D.1), to ensure comparability between the model and the data. Moreover, to guarantee an equal weighting of the wavelength bands during the model fitting, we imposed a lower limit on the errors: a minimum of 5 % (of the data) for the total spectrum as well as the correlated fluxes, and 5° for the closure phases. For faster computation, we applied a spectral binning with a window size of  $\Delta\lambda = 0.2\text{ }\mu\text{m}$  for the  $H$  and  $K$  bands, and  $\Delta\lambda = 0.1\text{ }\mu\text{m}$  for the rest.

### 4.1. Dust opacity model

We determined the opacity of disc material around HD 142527 A from a fit to the total  $N$ -band spectrum. This was not a quantitative analysis of the dust spectroscopy, but we sought to achieve a well-fitting opacity in the wavelength range used for the disc model (Sect. 4.2.2). The dust opacity model for this (see [van Boekel et al. 2005](#)) is described in Appendix E. The resulting best-fit dust composition<sup>5</sup> is presented in Table E.1 and shown in Fig. 1.

The HD 142527 system is unresolved in the total spectrum and cannot provide insight into the local dust composition and distribution of the disc. Contrary, the correlated fluxes provide spatial information on the dust composition (e.g. [Varga et al. 2024](#)). Nevertheless, for simplicity, we chose to keep the silicate mineralogy spatially constant in our modelling, and only allow changes to a silicate-to-carbonaceous ratio (Eq. 4). For this reason, our disc models are not able to reproduce the mineralogy gradient of the correlated fluxes (Fig. A.4).

<sup>5</sup>In-depth analysis from [van Boekel et al. \(2005\)](#) and/or [Juhász et al. \(2010\)](#) (both using grains computed via the DHS method) find dust compositions significantly different from ours.

## 4.2. Model components

Our disc models consists of a central star (i.e. a point source, see Sect. 4.2.1), an asymmetric temperature-gradient disc (Sect. 4.2.2), and an off-centre Gaussian component (Sect. 4.2.3), whose complex correlated fluxes  $\mathfrak{F}_v(q')$ <sup>6</sup> are derived below. The computation of the observables from the complex correlated flux is shown in Appendix F. An in-depth description of all applied models follows in Sect. 4.3.

### 4.2.1. Star

The primary star is the central component of the disc model. Because the star has an estimated angular diameter of only  $\approx 0.23$  mas (see Appendix D) it remains spatially unresolved in our observations and we treat it as a point source whose complex correlated flux is given by:

$$\mathfrak{F}_{v,\star} = F_{v,\star} \exp(2\pi i q'(\alpha \cos(\psi) + \beta \sin(\psi))), \quad (1)$$

where  $\alpha, \beta$  are the angular coordinates (in radians) of the image plane (in direction of right ascension (RA), declination (DEC), respectively), and  $\psi$  is the angle corresponding to the de-projected, spatial frequency  $q'$ . For the fitting procedure, we use the polar representation of the angular coordinates, where  $\rho$  is the separation from the centre and the position angle  $\Phi$  (east of north) (Berger & Segransan 2007). The derivation of the stellar flux  $F_{v,\star}$  is given in Appendix D.1.

### 4.2.2. Asymmetric temperature-gradient disc

The disc model consists of one or more zones surrounding the primary star. Such a zone (denoted by the index  $n$ ) is the result of integrating over infinitesimally thin rings (see Berger & Segransan 2007) with an emergent intensity  $I_{v,n}$ . The rings making up the zones can have an additional azimuthal modulation (Lazareff et al. 2017). Starting from a power-law approach, we now describe the emergent intensity and subsequently demonstrate how it connects to the complex, correlated flux.

We require the source function  $B_v(T)$  to determine the intensity of the zone. The source function depends on a temperature distribution:

$$T(r) = T_0 \left( \frac{r}{R_0} \right)^q. \quad (2)$$

The radial behaviour of the temperature profile is determined by its power-law index  $q$ , where  $T_0$  is the temperature at a reference radius of  $R_0 = 1$  au. If there is more than one zone, they share a single temperature profile. Moreover, we need the emissivity  $\epsilon_{v,n}$  to describe the intensity. The emissivity is made up by an optical depth  $\tau_{v,n}$  that, in turn, depends on the surface density of the zone:

$$\Sigma_n(r) = \Sigma_{0,n} \left( \frac{r}{R_0} \right)^{p_n}. \quad (3)$$

This is another power law, with  $\Sigma_{0,n}$  being the surface density at the reference radius  $R_0$ , and  $p_n$  its power-law index. Combined with the absorption-opacity curve of the silicates  $\kappa_{v,\text{abs,sil}}$ ,

<sup>6</sup>For brevity's sake, we shorten the de-projected spatial frequency  $q' = q'(i, \theta)$  and completely omit it as parameter of the complex correlated flux from now on.

the carbonaceous grain continuum  $\kappa_{v,\text{abs,cont}}$ , and the mass fraction  $w_{\text{cont},n}$ , we obtain the vertical optical depth

$$\tau_{v,n}(r) = \Sigma_n(r)[(1 - w_{\text{cont},n})\kappa_{v,\text{abs,sil}} + w_{\text{cont},n}\kappa_{v,\text{abs,cont}}]. \quad (4)$$

When accounting for inclination effects, the vertical optical depth changes to be along the line of sight, and we obtain the emissivity in the form of

$$\epsilon_{v,n}(r) = 1 - e^{-\tau_{v,n}(r)/\cos(i)}. \quad (5)$$

This quantity, multiplied by the radially dependent source function, gives the emergent intensity of the zone

$$I_{v,n}(r) = \epsilon_{v,n}(r)B_v(T(r)). \quad (6)$$

From Lazareff et al. (2017) we obtain the complex correlated flux for an azimuthally modulated, infinitesimally thin ring:

$$\mathfrak{F}_{v,\text{ring},n} = \sum_{m=0}^{\ell} (-i)^m A_{n,m} \cos(m(\psi - \phi_{n,m})) J_m \left( \frac{2\pi q' v}{c} r \right). \quad (7)$$

Here,  $J_m$  is the Bessel function of the first kind of order  $m$ ,  $A_{n,m}$  the modulation amplitude, and  $\phi_{n,m}$  the modulation angle. All orders up to  $\ell$  contribute to the ring, with  $\ell \geq 1$  introducing an azimuthal asymmetry and  $\ell = 0$  being the symmetric case (i.e.  $J_0$  with  $A_{n,0} = 1$ ). Using the intensity of Eq. (6) and integrating over the solid angle  $\Omega$  yields the complex correlated flux for the azimuthally modulated disc zone

$$\mathfrak{F}_{v,n} = 2\pi \cos(i) \int_{R_{\text{in},n}}^{R_{\text{out},n}} \mathfrak{F}_{v,\text{ring},n} I_{v,n}(r) r \, dr. \quad (8)$$

The zone extends from an inner radius  $R_{\text{in},n}$  to an outer radius  $R_{\text{out},n}$ . For this component, we used the ALMA observations of the outer disc from Bohn et al. (2022) in combination with the misalignment ( $\Delta\theta_{\text{in-out}} = 70^\circ$ ) from Marino et al. (2015) (see also Table 1) to compute<sup>7</sup> the inclination of the inner disc, and fix the inclination to  $i_{\text{in}} = 32^\circ 05$  and the position angle to  $\theta_{\text{in}} = 352^\circ$ . The computation was done as Nowak et al. (2024) pointed out that Bohn et al. (2022) used an unusual angle convention, which for HD 142527 seems not to agree with observed shadows cast by the inner onto the outer disc.

### 4.2.3. Gaussian

The behaviour seen in the correlated fluxes (i.e. the zero-crossing, see Sect. 3) hints at a more spatially confined asymmetric component. For this, we choose an off-centre Gaussian whose complex correlated flux (given by Berger & Segransan 2007) we multiply with a source function  $B_v(T(\rho))$ , a scale factor  $f$ , and the emissivity  $\epsilon_v$ :

$$\mathfrak{F}_{v,\text{Gauss}} = f \epsilon_v B_v(T(\rho)) \exp\left(-\frac{(\pi a q')^2}{4 \ln 2}\right). \quad (9)$$

Here, the temperature is computed via Eq. (2), the power-law of the accompanying disc component(s)  $T(r)$  at the position  $\rho$  of the Gaussian. The size of the Gaussian is given by the full width at half maximum (FWHM)  $a$ . The emissivity is identical to that from Eq. (5) with the difference that  $\Sigma$  is a direct fit parameter and not derived from a power-law.

As we cannot resolve this component and assume it to be compact, we fixed the FWHM at  $a = 2.57$  mas ( $= 0.41$  au for  $d = 159.3$  pc). This choice allows for enough flux to reproduce the signatures seen in the data while keeping the component unresolved in the  $N$  band.

<sup>7</sup>For this computation, we rearranged and recursively solved Eq. (7) from Bohn et al. (2022):

$$i_{\text{in}} = \arccos[(\cos(\Delta\theta_{\text{in-out}}) - \sin(i_{\text{in}}) \sin(i_{\text{out}}) \cos(\theta_{\text{in}} - \theta_{\text{out}})) / \cos(i_{\text{out}})]$$

### 4.3. Model geometries

The following section provides an explanation of the modelling approaches employed in this work. At the centre of each model is a point source (Sect. 4.2.1) representing HD 142527 A. The companion HD 142527 B, being 4.5 mag fainter than the primary in the  $H$  band (see Lacour et al. 2016), showing no definite signal in our data, was not included in the model.

There has been evidence of a gapped disc around HD 142527 A (e.g. Menu et al. 2015). For this reason, we first compared two azimuthally symmetric disc models (Sect. 4.2.2) to each other: a one-zone (i.e. continuous) vs. a two-zone (i.e. gapped) disc model. With this symmetric approach, the gapped model yielded the best fit to the data.

To reproduce the large closure phases in the  $N$  band (Sect. 3), we had to introduce an asymmetry. For this, we chose the simplest asymmetric model; an azimuthal modulation of first order ( $\ell = 1$ ). With this asymmetric two-zone disc model, we find three things: first, the large errors on the closure phases of the  $H/K$ , and  $L$  band did not allow us to constrain the modulation of the inner zone, even though the formal goodness of the fit improved. Furthermore, the closure phases of these bands show only a weak signal. This wavelength region is dominated by the innermost disc, and for these reasons, and to reduce the number of free parameters, we removed the modulation of the inner zone and only kept that of the outer zone. Second, a ‘global’ asymmetry does not adequately reproduce all our visibility and phase signals, particularly the zero-point crossing (the most robust feature of our data set; see Fig. A.4), immune to any systematics or calibration issues. We suspect that fitting this feature requires a more localised, smaller asymmetric emission than the global  $\ell = 1$  modulation. Third, we find that a fit to all  $N$ -band data simultaneously results in a worse  $\chi^2$  than fitting the individual  $N$ -band epochs with epoch-dependent parameters. This suggests a temporal variability in the  $N$ -band intensity distribution.

Therefore, we attempted a simple, localised asymmetric emission, specifically an off-centre Gaussian. With this phenomenological modelling approach, we find significantly better fits than with the first-order modulation. Similarly to before, fits to the individual epochs yield better results than fitting one model to all epochs concurrently. This consolidates the assumed temporal variability, which we interpret in Sect. 5.2.

Given our limited  $(u, v)$  coverage per epoch and the evidence for temporal variability, we do not attempt to fit more complex model geometries.

## 5. Discussion

### 5.1. The role of the stellar companion

Calculating the orbit of the companion HD 142527 B using the parameters from Nowak et al. (2024) listed in Table 1, we see that the three  $N$ -band UT observations are close in time to the periapsis passage (Fig. 2). We suggest that this close passage, combined with the short orbital period ( $\sim 24$  yr), heavily affects the disc and causes a complex and time-variable disc structure.

To infer the direct effect the companion has on the disc of the primary, we compute the Hill radius (Eggleton 1983; Hamilton & Burns 1992)

$$R_H \approx a(1 - e) \sqrt[3]{\frac{M_B}{3(M_A + M_B)}}. \quad (10)$$

Here,  $a$  is the semi-major axis,  $e$  the eccentricity, and  $M_A, M_B$ , the mass of the primary and secondary, respectively. Using the

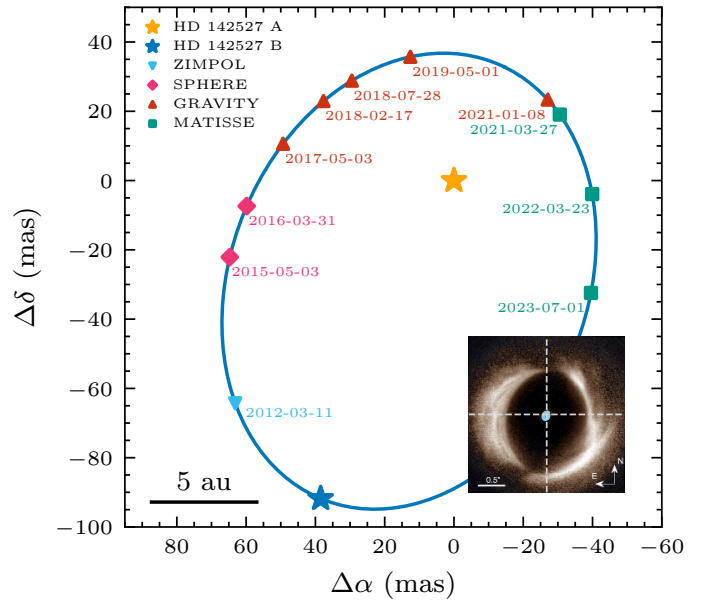


Fig. 2: System sketch. The host star HD 142527 A (orange star) orbited by its companion HD 142527 B (blue star at apoapsis). The orbit (blue) was computed using parameters from Nowak et al. (2024). The same parameters were used to derive the positions of the MATISSE points (teal squares). *Bottom right*: observation with SPHERE of the outer disc (Avenhaus et al. 2017) with the orbit (light blue) of the companion indicated.

stellar parameters from Table 1, Eq. (10) results in  $R_H \approx 2$  au, which is almost half the separation between the primary and the secondary ( $\sim 5$  au). This greatly affects the disc ( $r_{\text{out}} \lesssim 6$  au) and, most likely, causes complex structures. Additionally, the perturbations caused by interactions with the secondary potentially deplete the disc of material, requiring replenishment processes to explain the continued existence of the disc (e.g. streamers, see Casassus et al. 2015).

A time-variable asymmetry could also be induced by the companion in other ways, such as the companion heating the mid-plane of the disc or via shock processes. This would also explain the high crystallinity observed in HD 142527, by providing temperatures high enough to crystallise additional dust farther away from the primary (Harker & Desch 2002; van Boekel et al. 2004). This scenario is also supported by the SPHERE observations of Avenhaus et al. (2017), which found complicated emission just outside 4 au.

### 5.2. Nature of the asymmetry

To explore the prominent  $N$ -band asymmetry, we follow up on the step-by-step evolution of our modelling approaches as described in Sect. 4.3 and show how time-variable models, which allow for the possibility of interactions between the disc and companion (Sect. 5.1), yield the best results. Table 2 shows this by comparing the fit-goodness of the different model geometries.

Completely symmetric models (e.g. M1) are not able to reproduce the non-zero closure phases seen in our  $N$ -band observations. First, we asserted that a gapped disc (i.e. two-zone disc) model could be a good fit to the data. This is supported by the vanishing silicate feature of the correlated fluxes for some spatial frequencies (Figs. A.1 and A.4), which is similar to what

Table 2: Comparison of fit goodness (i.e.  $\chi^2_{r, \text{tot}}$ ) per model.

	M1	M2	M3
All epochs	10.54	8.26	4.47
Epoch 1	10.54	5.50	2.44
Epoch 2	10.54	7.30	1.89
Epoch 3	10.54	3.07	1.64

**Notes.** For the calculation of these values, see Appendix B. *First row*: time-invariant models fit to all data simultaneously. *Second to last row*: the same models with additional free parameters per  $N$ -band epoch. ‘M1’: symmetric (time-invariant) two-zone disc model; ‘M2’: M1 with an asymmetry in the outer zone; ‘M3’: one-zone disc model with an off-centre Gaussian asymmetry.

Varga et al. (2024) found for HD 144432, where a second component counteracted the silicate emission of the first. Considering the asymmetric two-zone model, another piece of evidence for a gap is the resolved component for the  $N$ -band correlated fluxes, as well as the decreasing closure phase at shorter wavelengths (Sect. 3), which indicates a less asymmetric structure closer to the star.

However, in Sect. 4.3, we noted that the zero-crossing, a very robust feature of our data, is not reproduced by the time-variable two-zone disc model, while the first and third epochs (2021 and 2023) are fairly well fitted. This suggests that the true intensity distribution on-sky exhibits a more spatially confined, off-axis emission component than a disc with a global cosine-like azimuthal intensity modulation can provide.

To explore this possibility, we created a model comprising a central star, an azimuthally symmetric disc component, and a relatively compact off-axis component. We assume that the off-axis component is too compact to be significantly spatially resolved in the  $N$  band, and for simplicity define it as a symmetric Gaussian with a FWHM of  $a \approx 2.6$  mas. The free parameters in this model are the position of the Gaussian component relative to the disc centre for each epoch, and the relative intensity for all epochs combined. With this approach, we are able to reproduce the zero-crossing in the 2022 epoch. This model is illustrated in Figs. 3 and 4, and the best fit parameters are given in Table 3.

We tested whether the angular position of the asymmetry is closely connected to the position of the companion<sup>8</sup> but find no clear correlation between the companion and the best-fit position of the asymmetry per epoch. Neither of the explored models fully reproduces the observations, and in either scheme, the asymmetric element in the model changes substantially from one epoch to the next, even between the second and third epochs, where the difference in the hour angle of the observations, and hence  $(u, v)$  coverage, is small. This suggests that the true intensity distribution is more complex than the models explored here, and that it varies on the  $\sim 1$  yr timescale that our observations probe.

With the limited  $(u, v)$  coverage of a single observation, fitting a model with significantly more complexity than the geometries explored here is not justified. At the same time, the temporal variability complicates the combination of observations gathered over several years. Objects like HD 142527 require ded-

Table 3: Parameters of the best-fit, time-dependent, one-zone disc model plus a Gaussian asymmetry (corresponds to model M3 in Table 2).

Parameter	Unit	Value
<b>FREE</b>		
$R_{\text{out}, 1}$	(au)	$5.32^{+0.07}_{-0.06}$
$w_{\text{cont}, 1}$	(%)	$79.30^{+0.98}_{-0.87}$
$\Sigma_{0,1}$	( $10^{-4}$ g cm $^{-2}$ )	$1.24^{+0.03}_{-0.02}$
$p_1$		$0.29 \pm 0.01$
$\log(f/\text{sr})$		$15.30 \pm 0.01$
$\rho_{\text{Gauss}, t0}$	(au)	$1.21 \pm 0.03$
$\rho_{\text{Gauss}, t1}$	(au)	$1.10 \pm 0.01$
$\rho_{\text{Gauss}, t2}$	(au)	$1.06^{+0.02}_{-0.01}$
$\Phi_{\text{Gauss}, t0}$	( $^{\circ}$ )	$150.11^{+2.02}_{-1.97}$
$\Phi_{\text{Gauss}, t1}$	( $^{\circ}$ )	$-125.34^{+1.49}_{-1.09}$
$\Phi_{\text{Gauss}, t2}$	( $^{\circ}$ )	$-154.24^{+1.62}_{-2.00}$
$\Sigma_{\text{Gauss}}$	( $10^{-4}$ g cm $^{-2}$ )	$16.90^{+0.56}_{-0.68}$
$w_{\text{cont, Gauss}}$	(%)	$60.71^{+36.86}_{-58.19}$
$T_0$	(K)	$599.74^{+2.61}_{-3.11}$
<b>FIXED</b>		
$R_{\text{in}, 1}$	(au)	0.1
$q$		-0.55
$d$	(pc)	159.3
$i_{\text{in}}$	( $^{\circ}$ )	32.05
$\theta_{\text{in}}$	( $^{\circ}$ )	352
$a$	(au)	0.41
$\chi^2_{r, F_v}$		4.13
$\chi^2_{r, F_{v, \text{corr}}}$		3.00
$\chi^2_{r, \Phi_{v, \text{cp}}}$		3.86
$\chi^2_{r, \text{tot}}$		3.36

**Notes.** For each parameter, the value is the median of the samples, with the uncertainties being the samples at 2.5 % and 97.5 %. The index  $t$  indicates a time-variability (‘t0’: epoch 2021, ‘t1’: epoch 2021, and ‘t2’: epoch 2023). All angles are given in the east of north direction.

icated imaging-like campaigns with the UTs, where data with good  $(u, v)$  coverage is collected within a time span  $\ll 1$  yr.

Nevertheless, our qualitative findings (i.e. a geometry deviating strongly from an azimuthally symmetric configuration, and with temporal variability on  $\lesssim 1$  yr timescales) provide useful insight into the gravitational interaction between the circum-primary disc and the low-mass stellar companion on its highly eccentric orbit. Price et al. (2018) presented simulations of this system<sup>9</sup> that have an inner disc which is heavily distorted at each periaxis passage of the companion, and which does not have time to ‘settle’ between periastron passages. The disturbance occurs ‘outside-in’, so that naturally the disc regions around 1 to a few au, to which our  $N$ -band observations are sensitive, are more strongly affected than the regions closer to the star probed by our  $L$  band observations. In the  $L$  band, we see a more sym-

<sup>8</sup> $\theta_B = 301.882, 264.368, 230.611$  east of north, for epoch 2021, 2022, and 2023, respectively.

<sup>9</sup>Available at <https://users.monash.edu.au/~dprice/pubs/HD142527>.

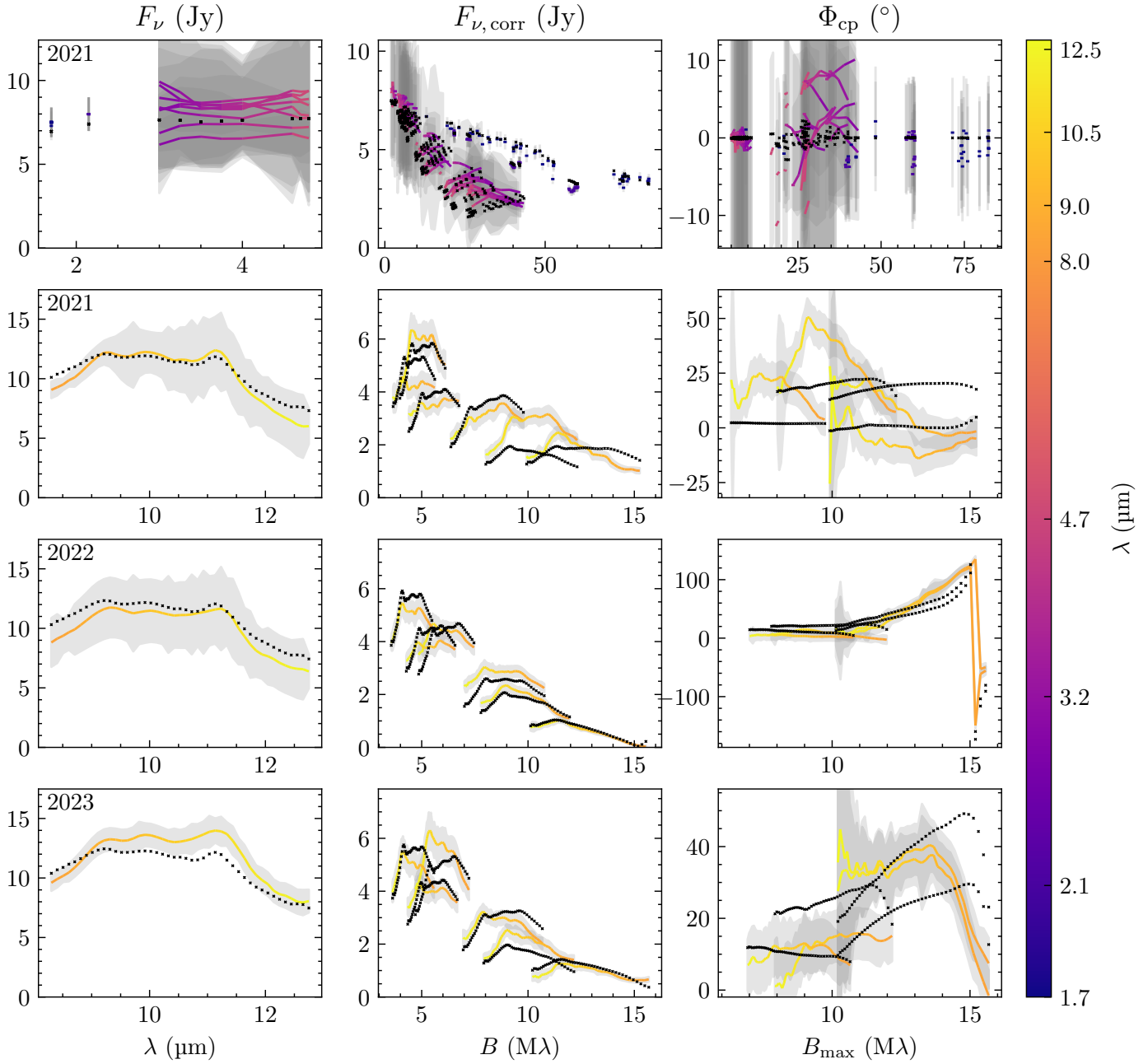


Fig. 3: Fit to data for the best-fit, one-zone disc model with an off-centre Gaussian asymmetry. The data (colored line) is overlaid with the model (black cross). The residuals of the plots are presented in Fig. G.1. *Left:* the total spectrum  $F_\nu$ . *Middle:* the correlated fluxes  $F_{\nu,\text{corr}}$ . *Right:* the closure phases  $\Phi_{\nu,\text{cp}}$ . *Top:* the PIONIER ( $H$  band), GRAVITY ( $K$  band), and MATISSE ( $L$  and  $M$  band) data. This data is fitted with all  $N$ -band data sets and shown, as an example, is the fit with the first  $N$ -band epoch. *Second row to bottom:* the first to third  $N$ -band epoch (2021, 2022, 2023).

metric, less distorted geometry, as indicated by the smaller closure phases compared to those in the  $N$  band. The orbital parameters of the HD 142527 system have been substantially revised since the work of Price et al. (2018), and the orbit found by Nowak et al. (2024) has both a shorter period and a closer periapsis distance than any of the configurations explored by the models of Price et al. (2018). A strongly distorted, temporally variable geometry is therefore likely, and we conclude that our observations provide qualitative support for this scenario, but stress the need for a dedicated interferometric imaging-like observation strategy with the UTs.

### 5.3. A very close-in rim

Throughout the different model geometries, we found the rim of the inner disc to consistently be at  $R_{\text{rim}} \approx 0.1$  au. Assuming a sublimation temperature of  $T_{\text{rim,literature}} = 1500$  K and plugging this, and the values from Table 1, into the formula for the inner rim/sublimation radius (Dullemond & Monnier 2010)

$$R_{\text{rim}} = \sqrt{\frac{L_\star}{4\pi\sigma T_{\text{rim}}^4}} = R_\star \left( \frac{T_\star}{T_{\text{rim}}} \right)^2 \quad (11)$$

the resulting sublimation radius is  $R_{\text{rim}} = 0.3$  au. Here,  $T_{\text{rim}}$  is the temperature at the inner rim of the disc,  $\sigma$  the Stefan-

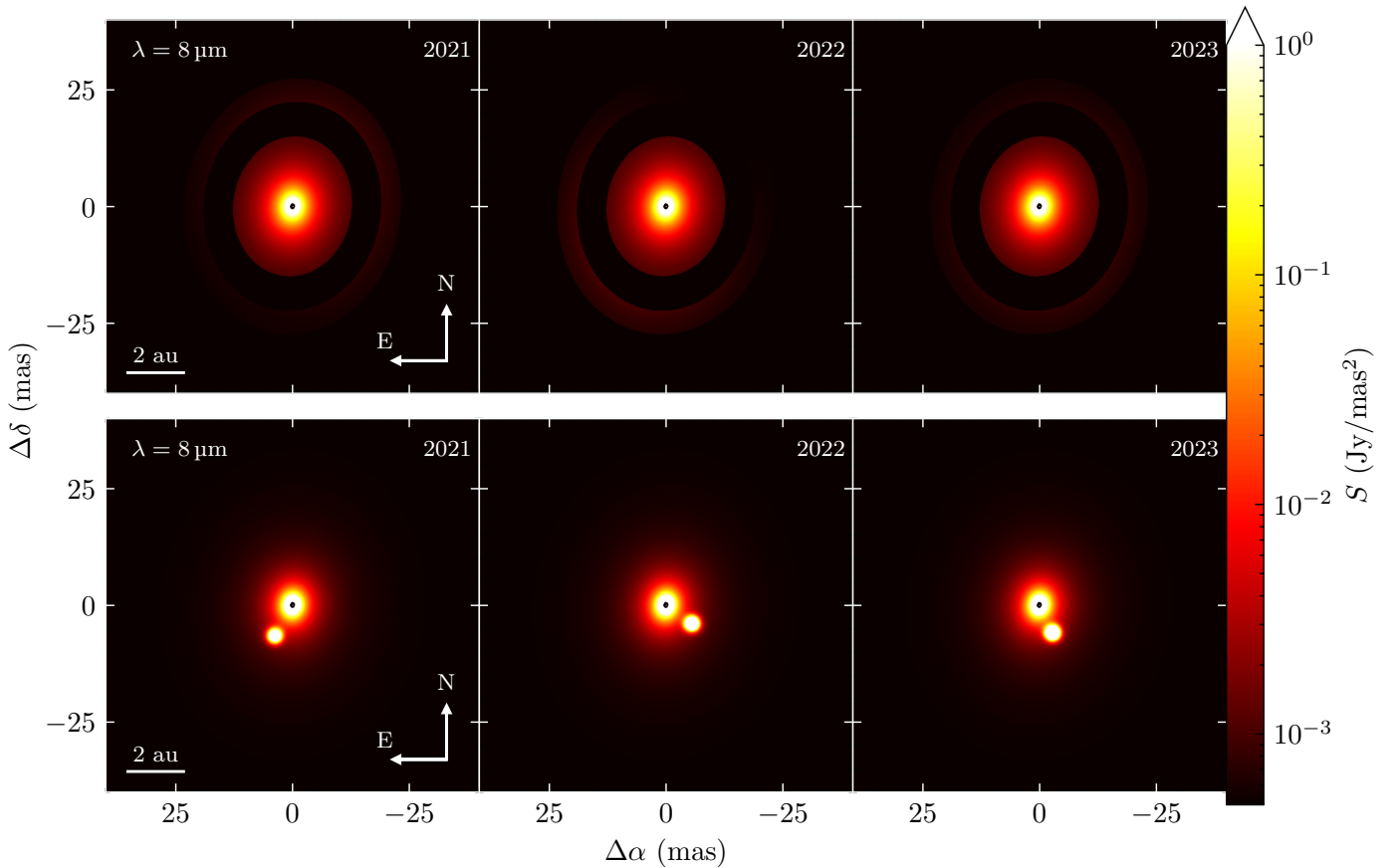


Fig. 4: Model images (in surface brightness). *Left to right*: the three epochs (2021, 2022, and 2023). *Top*: the two-zone disc model. *Bottom*: the best-fit, one-zone disc model plus a Gaussian.

Boltzmann constant, as well as the luminosity  $L_\star$ , the radius  $R_\star$ , and the effective temperature  $T_\star$  of the star. The sublimation radius computed from the theoretical assumption does not agree with that derived from our data. Such a close-in inner rim is, however, supported by earlier studies (e.g. Benisty et al. 2010b, 2011; Varga et al. 2024). These found either material beyond the sublimation radius and/or at hotter than expected temperatures. Furthermore, earlier studies on this target by the PIONIER (Lazareff et al. 2017) survey determined  $R_{\text{rim}} \approx 0.05$  au, and  $R_{\text{rim}} \approx 0.13$  au with the GRAVITY (GRAVITY Collaboration et al. 2019) survey. We compare the theoretically assumed temperature at the inner rim by computing the temperature at  $R_{\text{rim}} = 0.1$  au with the power-law of our best-fit model ( $T_0 = 599.74$  K and  $q = -0.55$ , see Table 3). This yields a sublimation temperature of  $T_{\text{rim}} \approx 2100$  K differing by  $\sim 600$  K from literature. The discrepancy between the calculation and the model fit may be caused by several factors. First, the assumed sublimation temperature  $T_{\text{rim,literature}} = 1500$  K, certainly, is an oversimplification as it does not account for the different types of dust grains (Gail 2004). There are various types of materials that sublimate at higher temperatures. Varga et al. (2024) and Flock et al. (2025) present different materials that could explain a close-in inner rim. For instance, corundum ( $T_{\text{rim}} \approx 1850$  K) or tungsten ( $T_{\text{rim}} \approx 2000$  K). However, from chemical equilibrium modeling by Varga et al. (2024) these species are expected to be present in too low abundances to result in observable spectral features, and indeed such features have not been observed. Moreover, in our modelling, we chose amorphous carbonaceous grains for the continuum. We

made this choice as these are featureless for the wavelengths used in this work. Iron would also fare better than carbonaceous grains (see Appendix E). Its presence in the inner regions is supported by observations of atomic jets that carry it (Assani et al. 2024; Caratti o Garatti et al. 2024), which require high speeds only available closer to the star. However, as it is featureless as well, we cannot distinguish it from carbonaceous grains in our modelling. Another possibility to explain the very close-in inner rim would be emission by hot gases. Benisty et al. (2010a) showed that for emission from hot gas in these regions, lines would need to be present in the spectral energy distribution (SED). We inspected archival X-shooter spectra of HD 142527 (Mendigutía et al. 2014; Fairlamb et al. 2015) for emission lines in the near infrared. We see hydrogen lines ( $\text{Br}_\gamma$ ,  $\text{Pa}_{\beta,\gamma}$ ) and a few weak, isolated lines that we did not identify. This is not consistent with dense gas being the dominant source of opacity in the inner disk region. For these reasons, it is most likely that dust survives farther inward and is picked up in our observations (e.g. Klarmann et al. 2017).

## 6. Summary and conclusions

In this paper, we introduced a chromatic and geometric disc model (Sect. 4) to probe the composition and the structure of the circumstellar disc around HD 142527 A. For this, we used photometric and interferometric data in the infrared covering a wide wavelength range; from archival observations of VLTI/PIONIER ( $H$  band) to observations of VLTI/GRAVITY ( $K$  band), and new data from our GTO VLTI/MATISSE ( $L$ ,  $M$ , and  $N$  band) survey.

Our key findings can be summarised as follows:

1. Our MATISSE data show large closure phases  $\Phi_{v,\text{cp}}$  and strong silicate features in both total spectra  $F_v$  and correlated fluxes  $F_{v,\text{corr}}$  (Sect. 3) confirming previous observations by [van Boekel et al. \(2005\)](#) and [Juhász et al. \(2010\)](#). The closure phase signals increase in amplitude from short to long wavelengths, while the silicate features grow weaker towards longer baselines and for some spatial frequencies disappear altogether.
2. The models we applied, either a two-zone disc (Sect. 4.2.2) with an asymmetry in the outer zone in the form of a first-order modulation, or a one-zone disc plus a localised asymmetry in the form of an off-centre Gaussian component (Sect. 4.2.3), cannot reproduce the  $N$  band of all epochs simultaneously. Only the best-fit model, the off-centre Gaussian, reproduces the robust zero-crossing measurement (epoch 2022, see Fig. 3).
3. We find the best fit to our data by implementing a time-dependent asymmetry for each  $N$ -band epoch, combined with the information of the shorter wavelength bands. To achieve this, the parameters defining the asymmetry have an iteration for each epoch, with the rest of the parameters being shared between all epochs (Sect. 5.1).
4. Combining the near-IR with the new  $L$ -band information, we can place the inner rim at  $R_{\text{rim}} \approx 0.1$  au (Sect. 5.3). This agrees well with previous findings from surveys of the  $H$  and  $K$  bands ([Lazareff et al. 2017](#); [GRAVITY Collaboration et al. 2019](#)) and leads to rim temperatures of  $T_{\text{rim}} \approx 2100 - 2200$  K for the one-zone plus a Gaussian and the two-zone disc model. However, by assuming a wall-like inner rim and a sublimation temperature of  $T_{\text{rim,literature}} = 1500$  K ([Dullemond & Monnier 2010](#)), the expected inner rim would be placed farther out at  $R_{\text{rim,literature}} = 0.3$  au.

From this, we conclude that:

1. The geometry of the circumstellar disc of the primary HD 142527 A is complex, substantially non-point symmetric, and temporally variable. Our best fit model shows no direct connection of the separation and/or position of the azimuthal asymmetry to the stellar companion HD 142527 B. However, the very complex state of the innermost disc region is, plausibly, caused by the close pass (see Fig. 2) and short orbit ( $P \approx 24$  yr) of the companion that, in conjunction with its large Hill radius of  $R_H \approx 2$  au, strongly perturbs the disc ( $r_{\text{out}} \lesssim 6$  au) around the primary (Sect. 5.1). This is supported by hydrodynamical simulations from [Price et al. \(2018\)](#).
2. We cannot wholly constrain the movement of the asymmetry or find a reasonable explanation for its position in conjunction with the time between epochs ( $\sim 1 - 1.3$  yr). This hints at the asymmetry being much more complex (such as multiple clumps, spirals, etc.), like found in other planet-forming discs (see [Setterholm et al. 2025](#)). Further study would require more sophisticated models (e.g. higher orders of modulation  $\ell > 1$  for the two-zone model) or image reconstruction. For both of these we lack sufficient data coverage to justify their application.
3. The difference between the spatial extent of the inner edge from the literature to our findings could be one or a combination of multiple causes. Such as, an oversimplified view of the sublimation radius (i.e. not accounting for different dust grain species, see [Gail 2004](#)), hot and dense gas ([Benisty et al. 2010a](#)), or material present farther inwards ([Klarman et al. 2017](#)). Examining X-shooter spectra

([Mendigutía et al. 2014](#); [Fairlamb et al. 2015](#)), we were able to exclude dense, hot gas as a potential source for the farther inward rim. Therefore, the inner rim of  $R_{\text{rim}} \approx 0.1$  au is, most probable, led back to a different dust composition or material farther inward.

Due to the complexity of the object, an in-depth study of the position/movement of the asymmetry would most likely require more data. This could be done with a dedicated MATISSE imaging-like campaign with the UTs obtained in a single epoch (ideally the same night, but at least the same period) and a denser sampling in  $(u, v)$  space (roughly 5 hour angles spaced by an hour). Additionally, the observations could be farther from the periapsis passage (e.g. around 2027, close to the apoapsis), potentially giving more insight into the effect the companion has on the disc. Moreover, radial velocity measurements (e.g. with the VLT/Echelle spectrograph for rocky exoplanet- and stable spectroscopic observations (ESPRESSO) instrument) would help in determining the orbiting speed and direction of the asymmetry.

## Data availability

The code used for data analysis and plotting, utilising the `oiplot` package (<https://zenodo.org/records/16727743>), is available at <https://zenodo.org/records/16723402>. And the model-fitting code from the `ppdmod` package at <https://zenodo.org/records/16728341>.

**Acknowledgements.** We thank the anonymous referee for their constructive and detailed comments, which significantly contributed to the improvement of this work. The MATISSE consortium is composed of multiple institutes: The Côte d’Azur observatory with the J-L Lagrange laboratory, the Institut national des sciences de l’Univers (INSU) at the Centre national de la recherche scientifique (CNRS), the University of Nice Sophia-Antipolis, the Max-Planck-institute for astronomy (MPIA), the Max-Planck-institute for radio astronomy (MPifr), the University of Kiel, the University of Leiden and the Nederlandse Onderzoekschool Voor Astronomie (NOVA), the University of Vienna, the University of Cologne, and the Konkoly observatory. GRAVITY has been developed in a collaboration by the Max-Planck-Institute for Extraterrestrial Physics, LESIA of Paris Observatory-PSL/CNRS/Sorbonne université/université Paris Cité and IPAG of Université Grenoble Alpes/CNRS, the MPIA, the university of Cologne, the Centro Multidisciplinar de Astrofísica Lisbon and Porto, and the ESO.

We also acknowledge the support of M. Fousneau and the [data science group](#) of the MPIA for their assistance with Bayesian inference.

This work was supported by CNRS/INSU, by the “Programme National de Physique Stellaire” (PNPS) of CNRS/INSU co-funded by CEA and CNES, and by Action Spécifique ASHRA of CNRS/INSU co-funded by CNES. This work has been supported by the French National Research Agency (ANR) in the framework of the “Investissements d’Avenir” program (ANR-15-IDEX-02) and in the framework of the “ANR-23-EDIR0001-01” project. J. Varga is funded from the Hungarian NKFIH OTKA project no. K-132406, and K-147380. This work was also supported by the NKFIH NKKP grant ADVANCED 149943. Project no. 149943 has been implemented with the support provided by the Ministry of Culture and Innovation of Hungary from the National Research, Development and Innovation Fund, financed under the NKKP ADVANCED funding scheme. J. Varga acknowledges support from the Fizeau exchange visitors programme. The research leading to these results has received funding from the European Union’s Horizon 2020 research and innovation programme under Grant Agreement 101004719 (ORP). F. Lykou acknowledges support from the NKFIH OTKA project no. K-147380.

Furthermore, this publication made use of the [national aeronautics and space administration \(NASA\) astrophysics data system \(ADS\)](#), the [set of identifications, measurements and bibliography for astronomical data \(SIMBAD\)](#) database, operated at Centre de données astronomiques de Strasbourg (CDS), and the [GiDB](#) of the JMMC.

This work is based on observations collected at the European southern observatory under ESO programmes 190.C-0963(B), 190.C-0963(D), 190.C-0963(E), 190.C-0963(F) for VLTI/PIONIER; 098.D-0484(A) for VLTI/GRAVITY; and 106.21Q8.007, 108.225V.006, 108.225V.009, 108.225V.011, 111.254P.001, and 111.254P.002 for VLTI/MATISSE. In addition, we made use of data from the following surveys or libraries: the two micron all-sky survey (2MASS) ([Skrutskie et al. 2006](#)), a joint project

of the university of Massachusetts and the Infrared Processing and Analysis Center (IPAC)/California institute of technology (Caltech), funded by NASA and the national science foundation (NSF); the **X-shooter spectral library** (Chen et al. 2014); the European space agency (ESA) mission **GAIA (GAIA)**, processed by the **GAIA data processing and analysis consortium (DPAC)**. Funding for the DPAC has been provided by national institutions, in particular the institutions participating in the GAIA multilateral agreement; and from WISE (Mainzer et al. 2011), a joint project of the University of California, Los Angeles, and the jet propulsion laboratory (JPL)/Caltech, and NEOWISE (Wright et al. 2010), a project of the JPL/Caltech. WISE and NEOWISE are funded by NASA.

This paper utilised the following software: the large language models (LLMs) **ChatGPT 4** (OpenAI et al. 2024), **DeepSeek-R1** (DeepSeek-AI et al. 2025), and **lumo 1.1** for code assistance/completion; **Aspro** of the JMMC. Furthermore, the following Python packages: **astropy** (The Astropy Collaboration et al. 2013, 2018, 2022); **astroquery** (Ginsburg et al. 2019, 2024); **corner** (Foreman-Mackey 2016; Dan Foreman-Mackey et al. 2024); **dynesty** (Speagle 2020); **matplotlib** (Hunter 2007); **numpy** (Harris et al. 2020); **oiplot** (Scheuck 2025a); **optool** (Dominik et al. 2021); **pandas** (McKinney 2010; The pandas development team 2025) with **openpyxl**; **ppdmod** (Scheuck 2025b); **scipy** (Virtanen et al. 2020; Gommers et al. 2025) from which the following functions were used: **j0** (wrapper of **Cephes** library), **jv** (wrapper of **AMOS** *zbesj* routine (Amos 1995)), and **gaussian\_kde** (Scott 2015; Silverman 2018; Bashtannyk & Hyndman 2001; Gray & Kish 1969); **SciencePlots** (Garrett et al. 2023); **tqdm** (Casper da Costa-Luis et al. 2024). Some of the acknowledgements were compiled using the **astronomy acknowledgement generator** with some of the software citation information being aggregated using the **software citation station** (Wagg & Broekgaarden 2024; Wagg et al. 2024).

## References

ALMA Partnership, Fomalont, E. B., Vlahakis, C., et al. 2015, *ApJ*, 808, L1  
 Amos, D. E. 1995, *ACM Trans. Math. Softw.*, 21, 388  
 Andrae, R., Schulze-Hartung, T., & Melchior, P. 2010, Dos and Don'ts of Reduced Chi-Squared  
 Andrews, S. M. 2020, *ARAA*, 58, 483  
 Andrews, S. M., Huang, J., Pérez, L. M., et al. 2018, *ApJL*, 869, L41  
 Assani, K. D., Harsono, D., Ramsey, J. P., et al. 2024, *A&A*, 688, A26  
 Avenhaus, H., Quanz, S. P., Schmid, H. M., et al. 2017, *AJ*, 154, 33  
 Bashtannyk, D. M. & Hyndman, R. J. 2001, *Computational Statistics & Data Analysis*, 36, 279  
 Benisty, M., Dominik, C., Follette, K., et al. 2023, Optical and Near-infrared View of Planet-forming Disks and Protoplanets  
 Benisty, M., Natta, A., Isella, A., et al. 2010a, *A&A*, 511, A74  
 Benisty, M., Renard, S., Natta, A., et al. 2011, *A&A*, 531, A84  
 Benisty, M., Tatulli, E., Ménard, F., & Swain, M. R. 2010b, *A&A*, 511, A75  
 Berger, J. P. & Segransan, D. 2007, *NAR*, 51, 576  
 Biller, B., Lacour, S., Juhász, A., et al. 2012, *ApJ*, 753, L38  
 Birnstiel, T. 2024, *ARAA*, 62, 157  
 Boccaletti, A., Folco, E. D., Pantin, E., et al. 2020, *A&A*, 637, L5  
 Boehler, Y., Weaver, E., Isella, A., et al. 2017, *ApJ*, 840, 60  
 Bohn, A. J., Benisty, M., Perraut, K., et al. 2022, *A&A*, 658, A183  
 Bouwman, J., Meeus, G., de Koter, A., et al. 2001, *A&A*, 375, 950  
 Buscher, D. F. & Longair, M. 2015, *Practical Optical Interferometry: Imaging at Visible and Infrared Wavelengths*, 1st edn. (Cambridge University Press)  
 Caratti o Garatti, A., Ray, T. P., Kavanagh, P. J., et al. 2024, *A&A*, 691, A134  
 Casassus, S., Marino, S., Pérez, S., et al. 2015, *ApJ*, 811, 92  
 Casassus, S., Van Der Plas, G., M. S. P., et al. 2013, *Nat*, 493, 191  
 Casper da Costa-Luis, Larroque, S. K., Altendorf, K., et al. 2024, *Tqdm: A Fast, Extensible Progress Bar for Python and CLI*, Zenodo  
 Chen, Y. P., Trager, S. C., Peletier, R. F., et al. 2014, *TM*, 158, 30  
 Choi, J., Dotter, A., Conroy, C., et al. 2016, *ApJ*, 823, 102  
 Christiaens, V., Casassus, S., Absil, O., et al. 2018, *A&A*, 617, A37  
 Claudi, R., Maire, A.-L., Mesa, D., et al. 2019, *A&A*, 622, A96  
 Cohen, M., Wheaton, Wm. A., & Megeath, S. T. 2003, *AJ*, 126, 1090  
 Cutri, R. M., Skrutskie, M. F., van Dyk, S., et al. 2003, *2MASS All Sky Catalog of Point Sources*.  
 Dan Foreman-Mackey, Adrian Price-Whelan, Vouzden, W., et al. 2024, *Dfm-Corner.Py: V2.2.3*, Zenodo  
 DeepSeek-AI, Guo, D., Yang, D., et al. 2025, DeepSeek-R1: Incentivizing Reasoning Capability in LLMs via Reinforcement Learning  
 Dominik, C., Min, M., & Tazaki, R. 2021, *ASCL*, ascl:2104.010  
 Dorschner, J., Begemann, B., Henning, T., Jaeger, C., & Mutschke, H. 1995, *A&A*, 300, 503  
 Dullemont, C. P. & Monnier, J. D. 2010, *ARAA*, 48, 205  
 Eggleton, P. P. 1983, *ApJ*, 268, 368  
 Fairlamb, J. R., Oudmaijer, R. D., Mendigutía, I., Ille, J. D., & Van Den Ancker, M. E. 2015, *MNRAS*, 453, 976  
 Fedele, D., Carney, M., Hogerheijde, M. R., et al. 2017, *A&A*, 600, A72  
 Fitzpatrick, E. L. & Massa, D. 2009, *ApJ*, 699, 1209  
 Flock, M., Chrenko, O., Ueda, T., et al. 2025, *A&A*, 701, A259  
 Foreman-Mackey, D. 2016, *JOSS*, 1, 24  
 Fukagawa, M., Tamura, M., Itoh, Y., et al. 2006, *ApJ*, 636, L153  
 Gaia Collaboration, Brown, A. G. A., Vallenari, A., et al. 2018, *A&A*, 616, A1  
 Gaia Collaboration, Brown, A. G. A., Vallenari, A., et al. 2021, *A&A*, 650, C3  
 Gaia Collaboration, Prusti, T., De Bruijne, J. H. J., et al. 2016, *A&A*, 595, A1  
 Gaia Collaboration, Vallenari, A., Brown, A. G. A., et al. 2023, *A&A*, 674, A1  
 Gail, H.-P. 2004, *A&A*, 413, 571  
 Garrett, J., Luis, E., H. -H. Peng, et al. 2023, *Garrettj403/SciencePlots: 2.1.1, Zenodo*  
 Garufi, A., Benisty, M., Pinilla, P., et al. 2018, *A&A*, 620, A94  
 Garufi, A., Meeus, G., Benisty, M., et al. 2017, *A&A*, 603, A21  
 Ginsburg, A., Sipőcz, B., Brasseur, C. E., et al. 2024, *AstroPy/Astroquery: V0.4.7, Zenodo*  
 Ginsburg, A., Sipőcz, B. M., Brasseur, C. E., et al. 2019, *AJ*, 157, 98  
 Gommers, R., Virtanen, P., Haberland, M., et al. 2025, *Scipy/Scipy: SciPy 1.16.0, Zenodo*  
 GRAVITY Collaboration, Abuter, R., Accardo, M., et al. 2017, *A&A*, 602, A94  
 GRAVITY Collaboration, Ganci, V., Labadie, L., et al. 2024, *A&A*, 684, A200  
 GRAVITY Collaboration, Perraut, K., Labadie, L., et al. 2019, *A&A*, 632, A53  
 GRAVITY Collaboration, Sanchez-Bermudez, J., Caratti O Garatti, A., et al. 2021, *A&A*, 654, A97  
 Gray, P. G. & Kish, L. 1969, *JRSS*, 132, 272  
 Guzmán-Díaz, J., Mendigutía, I., Montesinos, B., et al. 2021, *A&A*, 650, A182  
 Haffert, S. Y., Bohn, A. J., De Boer, J., et al. 2019, *Nat Astron*, 3, 749  
 Hamilton, D. P. & Burns, J. A. 1992, *Icar*, 96, 43  
 Harker, D. E. & Desch, S. J. 2002, *ApJ*, 565, L109  
 Harris, C. R., Millman, K. J., Van Der Walt, S. J., et al. 2020, *Nat*, 585, 357  
 Hauschildt, P. H., Barman, T., Baron, E., Aufdenberg, J. P., & Schweitzer, A. 2025, *A&A*, 698, A47  
 Henning, T. & Mutschke, H. 1997, *A&A*, 327, 743  
 Hunter, J. D. 2007, *CiSE*, 9, 90  
 Hunziker, S., Schmid, H. M., Ma, J., et al. 2021, *A&A*, 648, A110  
 Indebetouw, R., Mathis, J. S., Babler, B. L., et al. 2005, *ApJ*, 619, 931  
 Jaeger, C., Molster, F. J., Dorschner, J., et al. 1998, *A&A*, 339, 904  
 Juhász, A., Bouwman, J., Henning, Th., et al. 2010, *ApJ*, 721, 431  
 Keppler, M., Benisty, M., Müller, A., et al. 2018, *A&A*, 617, A44  
 Klarmann, L., Benisty, M., Min, M., et al. 2017, *A&A*, 599, A80  
 Kluska, J., Van Winckel, H., Coppée, Q., et al. 2022, *A&A*, 658, A36  
 Lacour, S., Biller, B., Cheetham, A., et al. 2016, *A&A*, 590, A90  
 Lazareff, B., Berger, J.-P., Kluska, J., et al. 2017, *A&A*, 599, A85  
 Lopez, B., Lagarde, S., Petrov, R. G., et al. 2022, *A&A*, 659, A192  
 Mainzer, A., Bauer, J., Grav, T., et al. 2011, *ApJ*, 731, 53  
 Marino, S., Perez, S., & Casassus, S. 2015, *ApJ*, 798, L44  
 Matter, A., Labadie, L., Kreplin, A., et al. 2014, *A&A*, 561, A26  
 McKinney, W. 2010, in *Python in Science Conference*, Austin, Texas, 56–61  
 Mendigutía, I., Fairlamb, J., Montesinos, B., et al. 2014, *ApJ*, 790, 21  
 Menu, J., van Boekel, R., Henning, Th., et al. 2015, *A&A*, 581, A107  
 Millour, F., Berio, P., Heininger, M., et al. 2016, in *SPIE Astronomical Telescopes + Instrumentation*, ed. F. Malbet, M. J. Creech-Eakman, & P. G. Tuthill, Edinburgh, United Kingdom, 990723  
 Min, M., Hovenier, J. W., & De Koter, A. 2005, *A&A*, 432, 909  
 Min, M., Waters, L. B. F. M., de Koter, A., et al. 2007, *A&A*, 462, 667  
 Müller, A., Keppler, M., Henning, Th., et al. 2018, *A&A*, 617, L2  
 Nowak, M., Rowther, S., Lacour, S., et al. 2024, *A&A*, 683, A6  
 OpenAI, Achiam, J., Adler, S., et al. 2024, *GPT-4 Technical Report*  
 Paunzen, E. 2022, *A&A*, 661, A89  
 Petrov, R. G., Allouche, F., Matter, A., et al. 2020, in *Optical and Infrared Interferometry and Imaging VII*, ed. A. Mérand, S. Sallum, & P. G. Tuthill (Online Only, United States: SPIE), 19  
 Pinte, C., Van Der Plas, G., Ménard, F., et al. 2019, *Nat Astron*, 3, 1109  
 Pohl, A., Benisty, M., Pinilla, P., et al. 2017, *ApJ*, 850, 52  
 Price, D. J., Cuello, N., Pinte, C., et al. 2018, *MNRAS*, 477, 1270  
 Riello, M., De Angeli, F., Evans, D. W., et al. 2021, *A&A*, 649, A3  
 Rubinstein, A. E., Macías, E., Espaillat, C. C., et al. 2018, *ApJ*, 860, 7  
 Rufener, F. & Nicolet, B. 1988, *A&A*, 206, 357  
 Scheuck, M. B. 2025a, *Oiplot, Zenodo*  
 Scheuck, M. B. 2025b, *Ppdmod, Zenodo*  
 Scott, D. W. 2015, *Multivariate Density Estimation: Theory, Practice, and Visualization*, 1st edn., Wiley Series in Probability and Statistics (Wiley)  
 Setterholm, B. R., Monnier, J. D., Baron, F., et al. 2025, *AJ*, 169, 318  
 Silverman, B. 2018, *Density Estimation for Statistics and Data Analysis*, 1st edn. (Routledge)

Skilling, J. 2004, in Bayesian Inference and Maximum Entropy Methods in Science and Engineering: 24th International Workshop on Bayesian Inference and Maximum Entropy Methods in Science and Engineering, Vol. 735 (AIP), 395–405

Skrutskie, M. F., Cutri, R. M., Stiening, R., et al. 2006, AJ, 131, 1163

Sogawa, H., Koike, C., Chihara, H., et al. 2006, A&A, 451, 357

Speagle, J. S. 2020, MNRAS, 493, 3132

Teague, R., Bae, J., Bergin, E. A., Birnstock, T., & Foreman-Mackey, D. 2018, ApJL, 860, L12

The Astropy Collaboration, Price-Whelan, A. M., Lim, P. L., et al. 2022, ApJ, 935, 167

The Astropy Collaboration, Price-Whelan, A. M., Sipőcz, B. M., et al. 2018, AJ, 156, 123

The Astropy Collaboration, Robitaille, T. P., Tollerud, E. J., et al. 2013, A&A, 558, A33

The pandas development team. 2025, Pandas-Dev/Pandas: Pandas, Zenodo

van Boekel, R., Min, M., Leinert, Ch., et al. 2004, Nat, 432, 479

van Boekel, R., Min, M., Waters, L. B. F. M., et al. 2005, A&A, 437, 189

Varga, J., Ábrahám, P., Chen, L., et al. 2018, A&A, 617, A83

Varga, J., Hogerheijde, M., Van Boekel, R., et al. 2021, A&A, 647, A56

Varga, J., Waters, L. B. F. M., Hogerheijde, M., et al. 2024, A&A, 681, A47

Vioque, M., Oudmaijer, R. D., Baines, D., Mendigutía, I., & Pérez-Martínez, R. 2018, A&A, 620, A128

Virtanen, P., Gommers, R., Oliphant, T. E., et al. 2020, Nat Methods, 17, 261

Wagg, T. & Broekgaarden, F. S. 2024, Streamlining and Standardizing Software Citations with The Software Citation Station

Wagg, T., Broekgaarden, F. S., & Gültekin, K. 2024, TomWagg/Software-Citation-Station: V1.2, Zenodo

Woillez, J., Petrov, R., Abuter, R., et al. 2024, A&A, 688, A190

Wright, E. L., Eisenhardt, P. R. M., Mainzer, A. K., et al. 2010, AJ, 140, 1868

Zubko, V. G., Mennella, V., Colangeli, L., & Bussoletti, E. 1996, MNRAS, 282, 1321

## Appendix A: Observations

Table A.1: The HD 142527 observations used in this study.

HD 142527						Calibrator				
Date and Time (UTC)	Instrument	Seeing ('')	$\tau_0$ (ms)	Array: Stations	Band	$\Delta$ Time (h:mm)	Name	LDD (mas)	Seeing ('')	$\tau_0$ (ms)
2013-02-20T08:14 <sup>†</sup>	PIONIER	0.8	3.1	M: D0-G1-H0-I1	H	$\sim\pm20$	HD142135	0.42	0.7	4.0
2013-06-04T04:53 <sup>†#</sup>	PIONIER	1.2	3.7	L: K0-A1-G1-J3	H	—	—	—	—	—
2013-06-06T02:16 <sup>†#</sup>	PIONIER	1.1	3.8	L: K0-A1-G1-J3	H	—	—	—	—	—
2013-06-07T01:39 <sup>†#</sup>	PIONIER	0.8	7.4	L: K0-A1-G1-J3	H	—	—	—	—	—
2013-06-10T01:08 <sup>†#</sup>	PIONIER	0.9	5.3	L: K0-A1-G1-J3	H	—	—	—	—	—
2013-06-15T02:57 <sup>†</sup>	PIONIER	1.4	2.2	M: D0-G1-H0-I1	H	$\sim\pm20$	HD 142386	0.24	1.3	1.3
2013-07-03T01:16 <sup>†#</sup>	PIONIER	1.4	2.7	S: D0-A1-C1-B2	H	—	—	—	—	—
2017-03-19T08:51 <sup>††</sup>	GRAVITY	0.7	8.0	L: A0-G1-J2-K0	K	+1:18	HD 143118	0.37	0.8	4.9
2019-03-23T09:06 <sup>‡</sup>	MATISSE	0.5	10.8	S: A0-B2-D0-C1	L	+0:13	* eps Sco	5.8	0.4	11.3
2019-05-06T04:00 <sup>‡</sup>	MATISSE	0.5	5.8	L: K0-G1-D0-J3	L	-0:13	HD 138742	1.2	0.7	5.6
2019-06-30T04:49	MATISSE	0.9	1.8	S: A0-B2-D0-C1	L	+0:30	* eps Sco	5.8	1.5	1.7
2021-03-08T07:52 <sup>‡</sup>	MATISSE	1.1	3.8	L: A0-G1-J2-J3	L	-0:27	HD139127	3.2	1.8	3.0
2021-03-11T06:47 <sup>‡</sup>	MATISSE	0.7	8.4	M: K0-G2-D0-J3	L	-0:26	HD139127	3.2	0.8	6.4
2021-03-16T06:50 <sup>‡</sup>	MATISSE	1.0	2.5	S: A0-B2-D0-C1	L	+0:26	* H Sco	4.7	1.4	1.7
2021-03-27T05:29	MATISSE	1.0	5.7	U: U1-U2-U3-U4	LN	-0:31	HD134505	2.5	1.0	7.3
2022-03-14T06:48	MATISSE	0.9	4.1	S: A0-B2-D0-C1	L	+0:26	* H Sco	4.7	0.8	4.1
2022-03-23T08:20	MATISSE	0.6	4.1	U: U1-U2-U3-U4	LN	-0:31	HD138816	2.1	0.7	3.8
2022-05-11T06:22	MATISSE	1.2	2.9	L: A0-G1-J2-J3	L	+0:29	HD149401	2.5	1.0	3.3
2023-05-14T04:25	MATISSE	0.8	4.4	S: A0-B2-D0-C1	L	-0:41	* ups Lib	4.6	1.4	2.8
2023-06-12T04:10 <sup>‡</sup>	MATISSE	0.7	2.5	S: A0-B2-D0-C1	L	-0:27	* ups Lib	4.6	0.8	3.4
2023-07-01T00:57	MATISSE	1.0	4.8	U: U1-U2-U3-U4	LN	-0:24	HD134505	2.5	1.2	4.5
2023-07-09T03:53	MATISSE	0.6	2.8	S: A0-B2-D0-C1	L	-0:27	* ups Lib	4.6	0.6	3.3
2023-07-12T00:36	MATISSE	1.6	0.8	S: A0-B2-D0-C1	L	-0:34	* ups Lib	4.6	1.8	1.3
2023-08-12T01:32	MATISSE	0.9	3.2	S: A0-B2-D0-C1	L	-0:28	* ups Lib	4.6	1.3	3.1

**Notes.** Indicated are the instrument, the date and time, the atmospheric conditions (the seeing and the coherence time  $\tau_0$ ), the array configuration with the corresponding stations, as well as the spectral band, and information on the calibrator. Observations highlighted in red were not used in this work. The letters before the colon in the "Array: Stations" column are abbreviations of the array configurations: "S" – small, "M" – medium, "L" – large, and "U" – UTs. For HD 142527, the seeing and the coherence time  $\tau_0$  given are the mean value during the observation, while for the calibrator they are the value at the start of the observations.

(<sup>†</sup>) Archival data obtained from OiDB (Lazareff et al. 2017). (<sup>††</sup>) Reduced and calibrated data obtained from GRAVITY Collaboration et al. (2019).

(#) No calibrator information was logged for the observation. (<sup>‡</sup>) Though good atmospheric conditions, this observation showed artifacts or a low S/N.

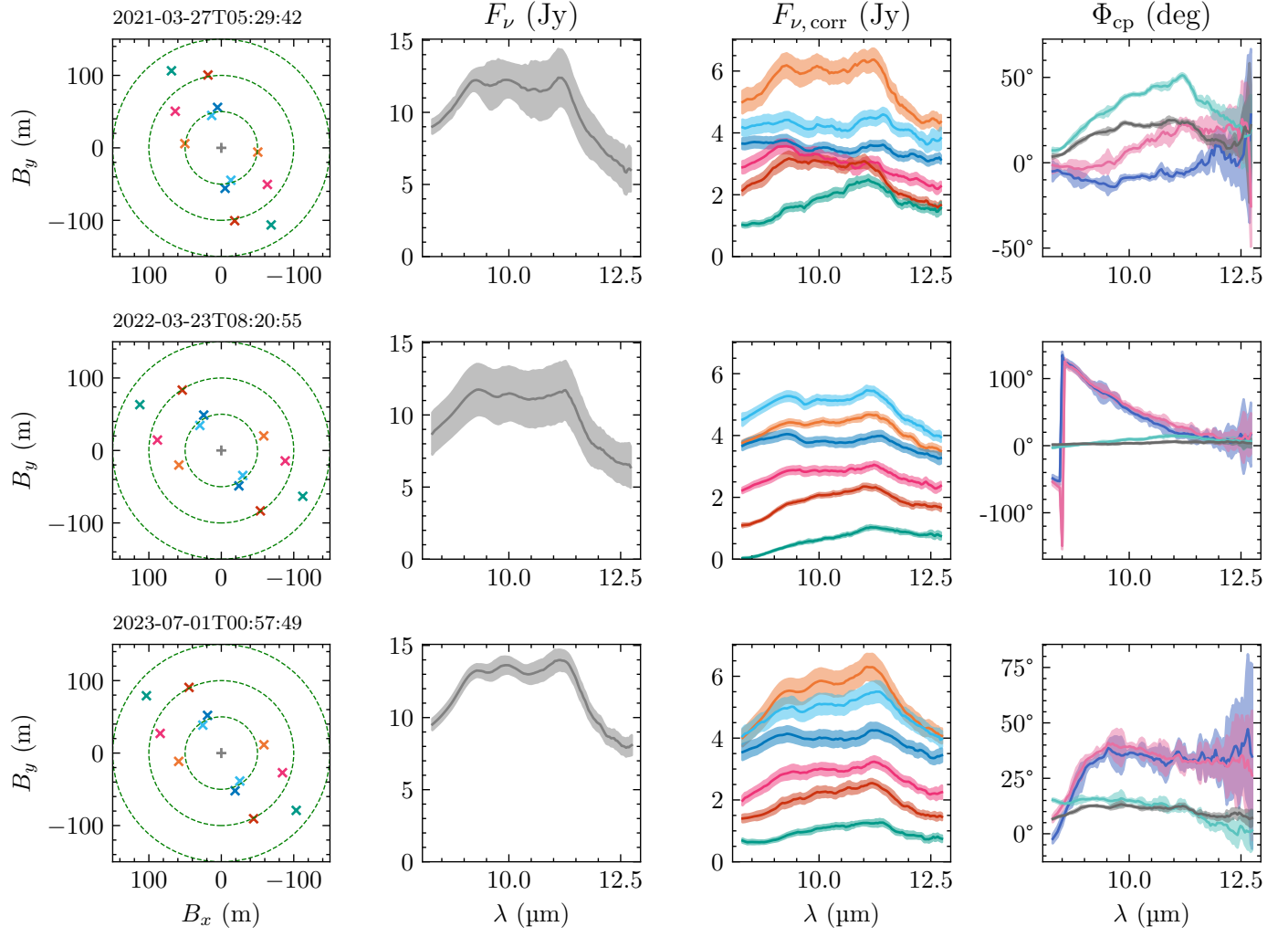


Fig. A.1: MATISSE  $N$ -band observations of HD 142527 (Table A.1). *Left to right:* the baseline distribution, the single dish spectra, the correlated fluxes, and the closure phases.

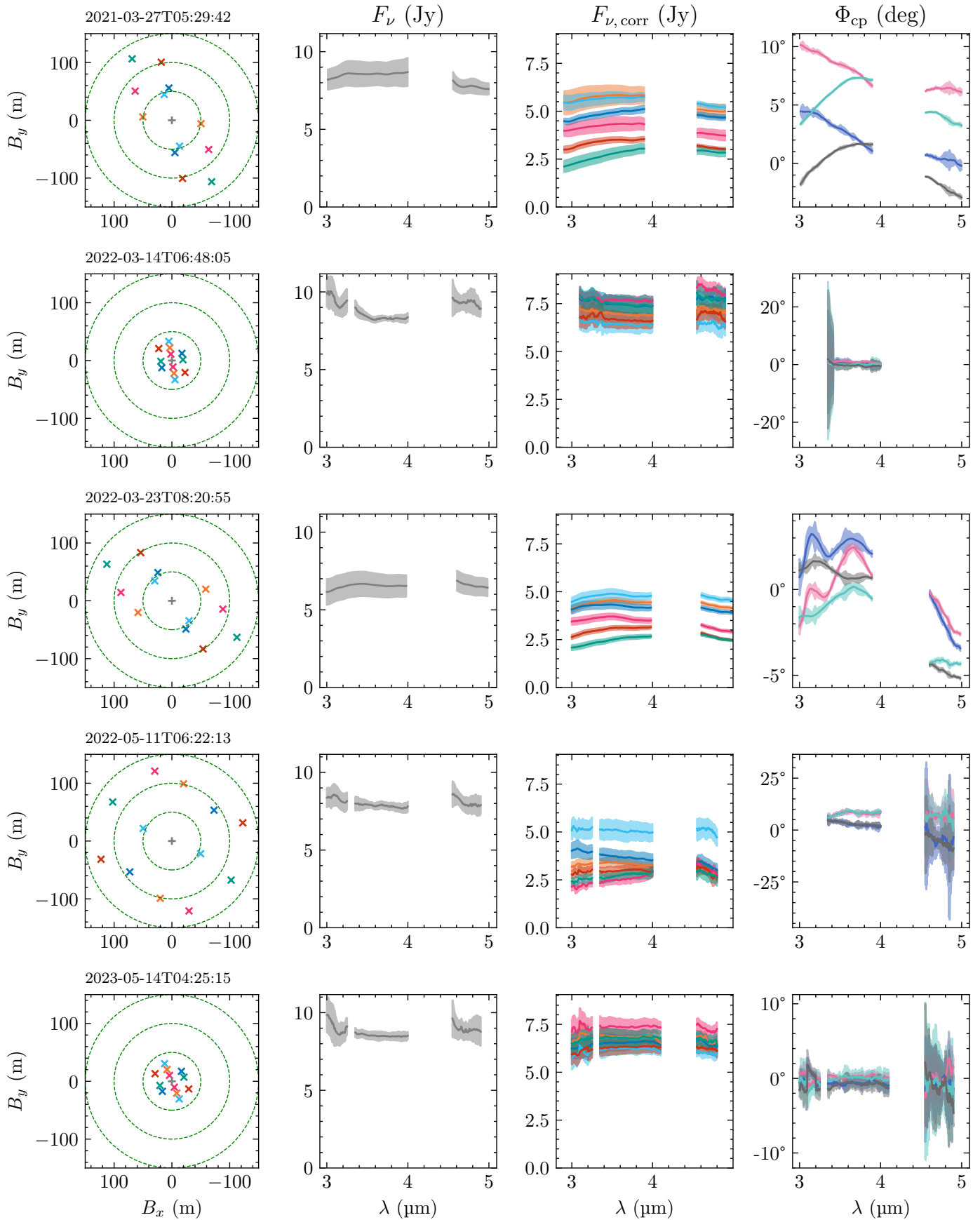


Fig. A.2: Individual  $L/M$ -band, MATISSE observations of HD 142527 (Table A.1). The layout is the same as in Fig. A.1. Single-dish spectra are from the chopped data, while the other observables are from the non-chopped mode. Emission peaks not relevant to this study, poor-quality data, and ranges outside the band windows were flagged.

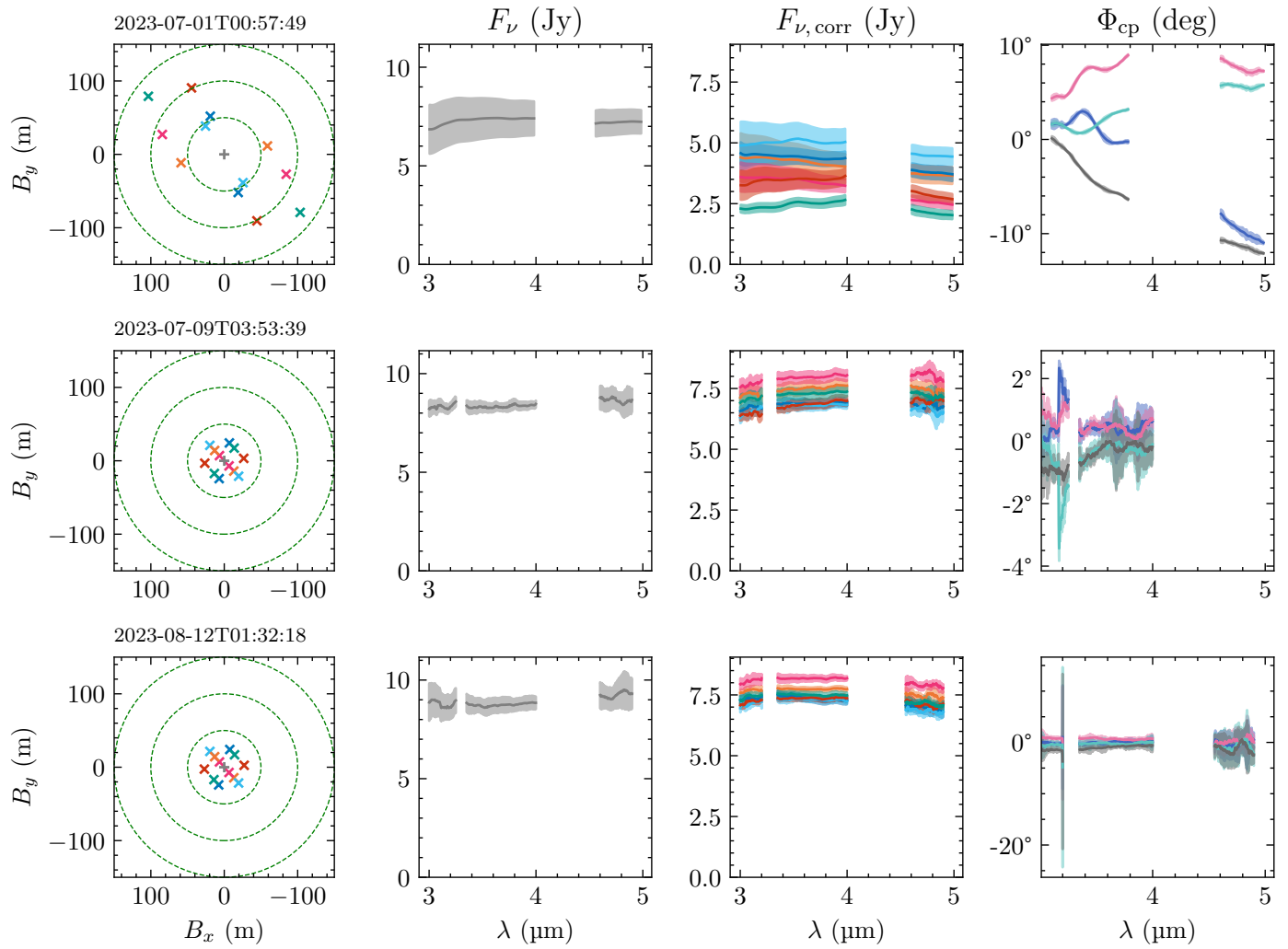


Fig. A.3: Continuation of Fig. A.2

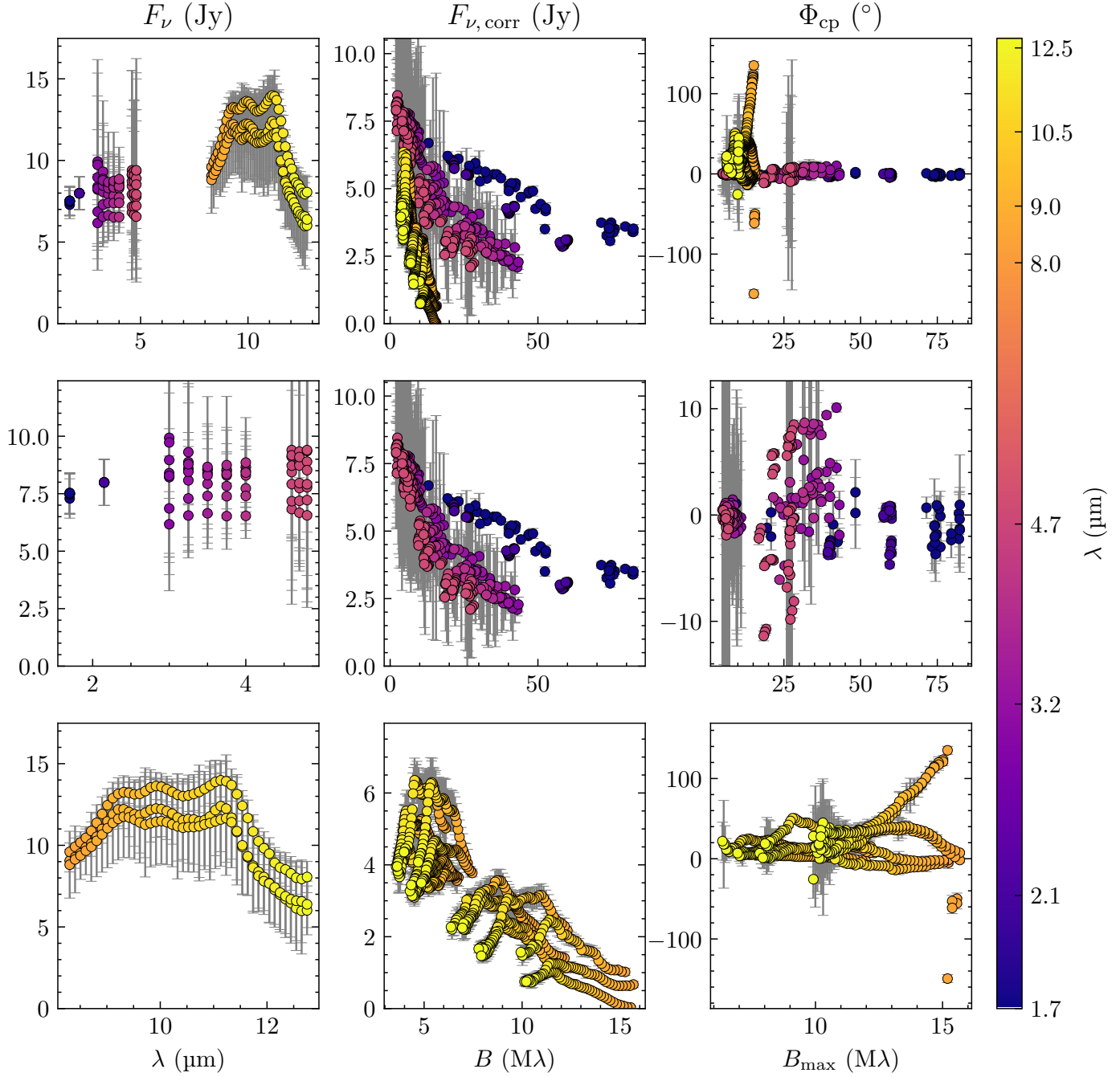


Fig. A.4: Overview of binned data used for model-fitting. *Left to right*: the three observables, the total spectrum, the correlated fluxes, and the closure phases. *Top to bottom*: the data from all bands (H, K, L, M, and N), a zoom-in to the bands of shorter wavelengths (H, K, L, and M), and a zoom-in to the N band.

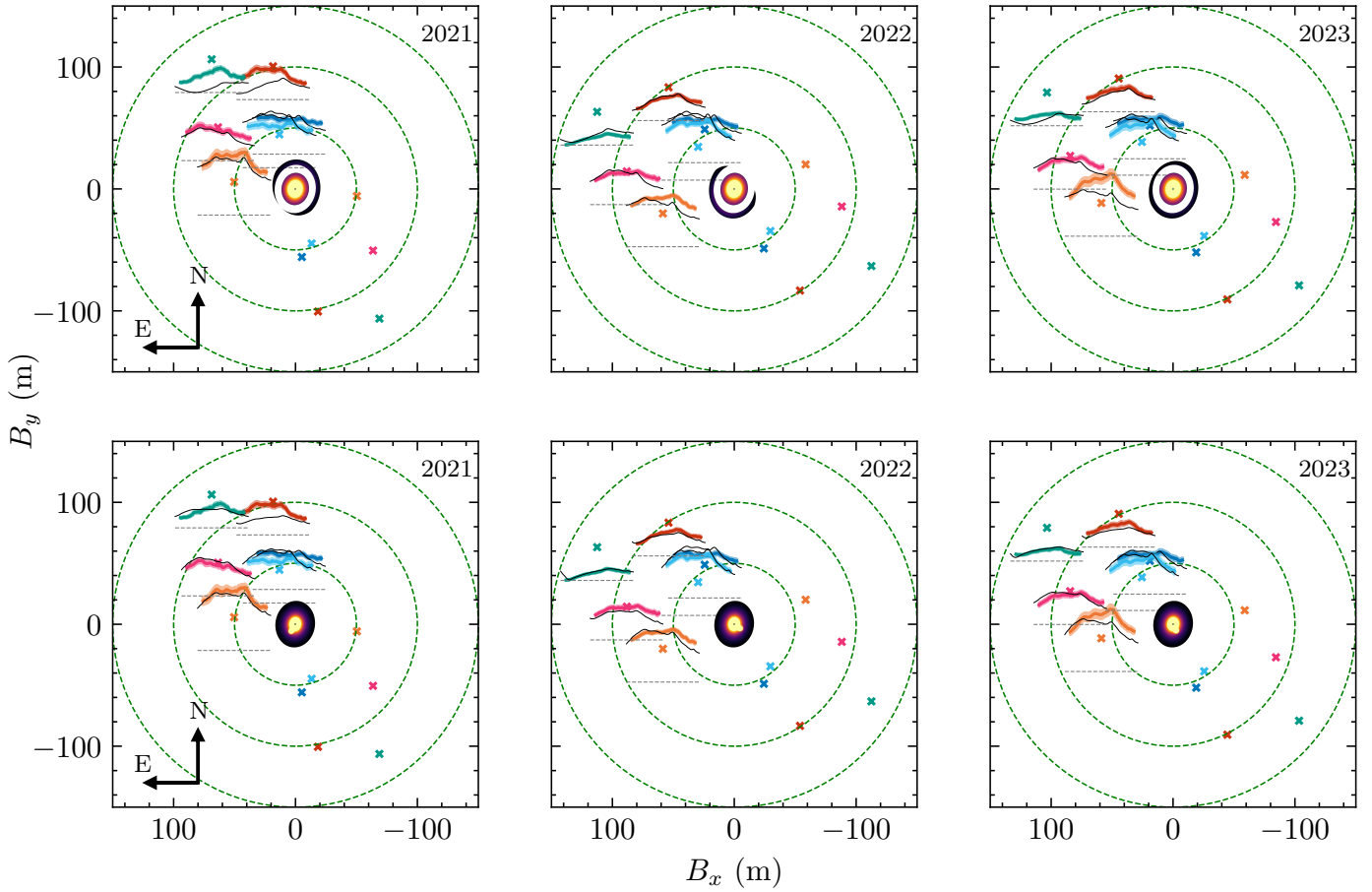


Fig. A.5: Data coverage of the baseline distribution of the  $N$ -band epochs is shown for each model. The correlated fluxes (coloured line) in the top-left corner are overlaid with the model (black line) at the baseline position (coloured cross). Each correlated flux curve is underlined (grey-dashed line), indicating the zero line of the y-axis. Equidistant contours of baselines (green-dashed circles; 50 m step width) are indicated. *Left to right*: the three  $N$ -band epochs (2021, 2022, 2023). *Top*: the two-zone disc model. *Bottom*: the one-zone disc model plus a Gaussian.

## Appendix B: Model fitting

To fit the model to our data, we chose Bayesian inference, more specifically, nested sampling. This algorithm efficiently samples the global parameter space (even if it is not well defined, which is typically a problem for Markov chain Monte Carlo (MCMC) methods) while avoiding getting stuck in local extrema. It samples by estimating the evidence

$$\mathcal{Z} \equiv P(\mathbf{D}|M) = \int_0^\infty X(x) dx = \int \mathcal{L}(X) dX, \quad (\text{B.1})$$

treating the integral of the posterior over all parameters as an integral over the prior volume

$$X(x) = \int_{\Theta: \mathcal{L}(\Theta) > x} \pi(\Theta) d\Theta \quad (\text{B.2})$$

instead. With this, it can then evaluate an iso-likelihood contour  $\mathcal{L}_i = \mathcal{L}(X_i)$  associated with samples from the prior volume and compute the evidence over ‘nested’ shells. At each iteration  $i$ , the remaining evidence in the prior volume is roughly bounded by  $\Delta\mathcal{Z}_i \approx \mathcal{L}_{\max} X_i$ . The difference between this and the current evidence  $\mathcal{Z}_i$

$$\Delta \ln \mathcal{Z}_i \equiv \ln(\mathcal{Z}_i + \Delta\mathcal{Z}_i) - \ln \mathcal{Z}_i \quad (\text{B.3})$$

serves as the stopping criterion (Skilling 2004; Speagle 2020).

For the likelihood, we use the least-squares minimisation

$$\mathcal{L}(\Theta) \equiv P(\mathbf{D}|\Theta, M) \equiv \chi^2(\Theta) = \sum_{n=1}^N \left( \frac{y_n - M(\Theta)}{\sigma_n} \right)^2. \quad (\text{B.4})$$

This enables the fitting of a model to data of  $N$  points  $y_n$  measured with (uncorrelated) errors  $\sigma_n$ . For the model comparison and to estimate the model-fit goodness, we also use the reduced form

$$\chi^2_r(\Theta) = \frac{\mathcal{L}(\Theta)}{N - N_\Theta}. \quad (\text{B.5})$$

The  $\chi^2_r$  takes the degrees of freedom (DOF)  $N - N_\Theta$  into account (Andrae et al. 2010). The number of model parameters  $N_\Theta$  may vary between epochs (i.e. time-variable parameters) and/or for each observable.

For the  $\mathcal{L}$ , the contributions from the total spectra, the correlated fluxes, and the closure phases are computed separately and then summed up

$$\mathcal{L}_{\text{tot}} = w_{F_\nu} \mathcal{L}_{F_\nu} + w_{F_{\nu,\text{corr}}} \mathcal{L}_{F_{\nu,\text{corr}}} + w_{\Phi_{\nu,\text{cp}}} \mathcal{L}_{\Phi_{\nu,\text{cp}}}. \quad (\text{B.6})$$

However, the  $\chi^2_{r,\text{tot}}$  is generally not a simple addition due to the above described change of DOF per observable and as the DOF for the whole model need to be taken into account.

We use the weights  $w$  only to equalise the observables with respect to the number of data points. Interferometric instruments at the VLTI have, per observation and frequency element  $\nu$ , the following distribution of data points for each observable

$$\begin{aligned} n_{\nu, F_\nu} &= N \vee 1, \\ n_{\nu, F_{\nu,\text{corr}}} &= \frac{N(N-1)}{2}, \quad \text{with} \quad \binom{N}{2}, \\ n_{\nu, \Phi_{\nu,\text{cp}}} &= \frac{N(N-1)(N-2)}{6}, \quad \text{with} \quad \binom{N}{3}. \end{aligned} \quad (\text{B.7})$$

Here,  $n_{\nu, F_\nu}$  is the number of flux measurements (often averaged to be 1),  $n_{\nu, F_{\nu,\text{corr}}}$  the number of baselines for the correlated flux, and  $n_{\nu, \Phi_{\nu,\text{cp}}}$  the number of triangles for the closure phases, with  $N$  being the number of telescopes.

## Appendix C: Model parameters

Table C.1 presents an overview of all the model parameters appearing in Sect. 4.

Table C.1: Model parameters.

Parameter	Unit	Description
<b>Dust opacity model</b>		
<b>FREE</b>		
$s$		Scaling factor
$T_c$	(K)	Charac. temperature
$w_k^a$		Contribution weight
$\kappa_{\nu,\text{abs},k}$	(cm $^2$ g $^{-1}$ )	Absorption opacity
<b>Stellar spectrum model</b>		
<b>FREE</b>		
$\theta$	(mas)	Apparent diameter
$A_V$	(mag)	Extinction value
<b>FIXED</b>		
$T_\star$	(K)	Temperature
$A_\lambda$	(mag)	Extinction curve
$g$	(m s $^{-2}$ )	Surface gravity
<b>Asymmetric disc</b>		
<b>FREE</b>		
$R_{\text{in},n}^b$	(au)	Inner radius
$R_{\text{out},n}$	(au)	Outer radius
$w_{\text{cont},n}$		Continuum weight
$\Sigma_{0,n}$	(g cm $^{-2}$ )	Surface density at $R_0$
$p_n$		Slope of surface dens.
$T_0$	(K)	Temperature at $R_0$
$q$		Temperature exponent
$A_{n,m}^c$		Modulation amplitude
$\phi_{n,m}$	( $^\circ$ )	Modulation angle
<b>FIXED</b>		
$i_{\text{in}}$	( $^\circ$ )	Inclination angle
$\theta_{\text{in}}$	( $^\circ$ )	Position angle
$R_0$	(au)	Reference radius
$\kappa_{\nu,\text{abs},\text{sil}}$	(cm $^2$ g $^{-1}$ )	Silicate opacity
$\kappa_{\nu,\text{abs},\text{cont}}$	(cm $^2$ g $^{-1}$ )	Continuum opacity
<b>Gaussian</b>		
<b>FREE</b>		
$f$		Scaling factor
$\rho$	(au)	Radial separation
$\Phi$	( $^\circ$ )	Position angle
$\Sigma$	(g cm $^{-2}$ )	Surface density
<b>FIXED</b>		
$a$	(au)	FWHM

**Notes.** <sup>(a)</sup> The index  $k$  denotes the dust stoichiometry. <sup>(b)</sup> The index  $n$  denotes the disc zone. <sup>(c)</sup> The index  $m$  denotes the modulation order.

## Appendix D: Stellar spectrum and parameters

In order to estimate the contribution of the stellar photosphere to our observed signals, we perform model atmosphere fitting to observed optical photometry of HD 142527, keeping the effective temperature  $T_\star = 6500$  K as derived by Fairlamb et al. (2015) from X-shooter spectroscopy, and using their spectroscopically derived surface gravity of  $\log g = 3.93$  as an initial value. We calculate synthetic photometry from a reddened PHOENIX model spectrum by Hauschildt et al. (2025) with the corresponding parameters, adopting solar composition. We then tune the apparent stellar diameter  $\theta$  and extinction value  $A_V$ , and calculate updated synthetic photometry until the best fit to the observed photometry is reached through  $\chi^2$  minimisation, keeping  $T_\star$  and  $\log g$  fixed. Adopting the GAIA distance, we then obtain an estimate of the stellar radius and luminosity. We compare these values to pre-main-sequence, evolutionary tracks by Choi et al. (2016) to obtain an estimate of the stellar mass and age. From the stellar radius and mass estimate, we obtain an updated estimate of the surface gravity, and we iteratively repeat the procedure using a PHOENIX model spectrum with the updated  $\log g$  value. We ultimately obtain a best-fit, reddened model atmosphere spectrum and a set of stellar parameters that are mutually consistent. The procedure is described in detail below.

### D.1. Method details

We adopt optical photometry in the Geneva system from Paunzen (2022) and from GAIA data release 3 (GAIA DR3) (Gaia Collaboration et al. 2016, 2023). We also consider infrared photometry from the 2MASS point source catalogue (Skrutskie et al. 2006; Cutri et al. 2003) and AllWISE catalogue (Wright et al. 2010; Mainzer et al. 2011), but these are ignored in the fit to the photosphere because they contain infrared excess emission from the circumstellar material. We adopt the spectro-photometric response curves  $R_\lambda$  for the Geneva system from Rufener & Nicolet (1988), for GAIA DR3 from Riello et al. (2021), for 2MASS from Cohen et al. (2003) and for AllWISE from Wright et al. (2010). The photometric zero-point calculation (i.e. the definition of  $\phi_{\lambda,0}$  for the respective bands) is done as follows: for the Geneva system, we adopt the alpha\_lyr\_mod\_002.fits model spectrum from the CALSPEC database<sup>10</sup> and the  $\alpha$  Lyr magnitudes from Table 11 of Rufener & Nicolet (1988); for GAIA DR3 we adopt the alpha\_lyr\_mod\_002.fits from the CALSPEC database, scaled to  $3.62286 \cdot 10^{-11} \text{ W m}^{-2} \text{ nm}^{-1}$  at 550 nm following Riello et al. (2021); for 2MASS we adopt a spectrum constant in  $wF_\lambda$  at values of  $3.129 \cdot 10^{-13}$ ,  $1.133 \cdot 10^{-13}$ , and  $4.283 \cdot 10^{-14} \text{ W m}^{-2} \mu\text{m}^{-1}$  in the  $J$ ,  $H$ ,  $K$  bands, respectively, following Cohen et al. (2003); for the AllWISE catalog we use an  $\alpha$  Lyr model by Martin Cohen, (Wright, private communication). All photometric facilities have detectors that are based on the photoelectric effect, so that:

$$m_i = -2.5 \log_{10} \left( \frac{\int_0^\infty \phi_\lambda R_\lambda d\lambda}{\int_0^\infty \phi_{\lambda,0} R_\lambda d\lambda} \right) \quad (D.1)$$

where  $m_i$  is the observed magnitude in photometric band  $i$ ,  $\phi_\lambda$  is the target spectrum expresses as photon flux (e.g. in units of  $[\gamma] = [\text{s}^{-1} \text{ cm}^{-2} \mu\text{m}^{-1}]$ ) and  $\phi_{\lambda,0}$  is the corresponding spectrum

that defines the photometric zero point of the respective band. The model photosphere spectrum  $\phi_\lambda$  is calculated as follows:

$$\phi_\lambda = \Omega I_{\lambda,0}(T_\star, \log g) \cdot 10^{-0.4A_\lambda} \quad (D.2)$$

where  $I_{\lambda,0}$  is the disc-integrated average surface brightness of the PHOENIX stellar model atmosphere without foreground extinction,  $\Omega = \pi\theta^2/4$  is the solid angle subtended by the star as viewed from Earth, and  $A_\lambda$  is the wavelength-dependent extinction curve adopted from Indebetouw et al. (2005) and Fitzpatrick & Massa (2009), scaled so that its value at 0.55  $\mu\text{m}$  matches the fit parameter  $A_V$ .

Note that in our photometric data, we measure the combined signal of the primary Herbig Ae star and the low-mass M-type companion, but we ignore the contribution of the latter in our analysis. Given the much lower luminosity and photospheric temperature of the companion compared to the primary, its emission should affect the optical fluxes at no more than the  $\approx 1$  % level.

### D.2. Fit results

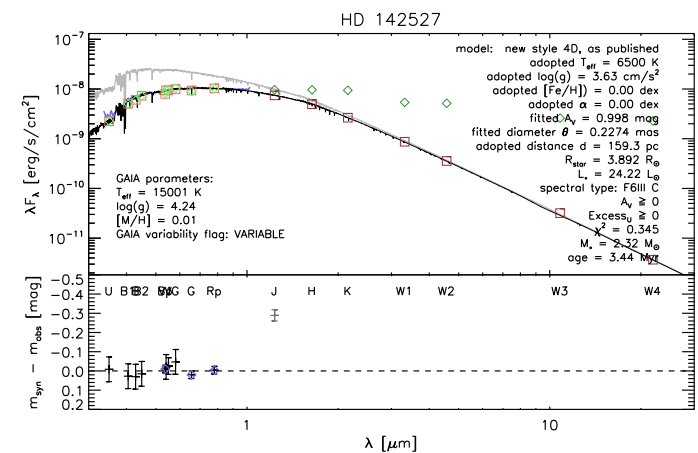


Fig. D.1: SED fit. *Top*: the best-fit stellar atmosphere model (black) with the zero-extinction model (grey) fitted to the observed photometry (green diamond) and the low-resolution GAIA XP spectrum (blue). The observed photometry is contrasted by the synthetic photometry (red squares). *Bottom*: the residuals of observed and synthetic magnitudes

From the resulting model atmosphere fit in Fig. D.1, the excess emission at near- and mid-IR wavelengths is evident as seen from divergence in observed and synthetic photometry. No scaling has been applied to the low-resolution GAIA XP spectrum, and the excellent match in flux levels illustrates both the validity of our method and the excellent absolute calibration of the GAIA spectra.

We find that we obtain an adequate fit to the spectrum when adopting the spectroscopically derived temperature of  $T_\star = 6500$  K (Fairlamb et al. 2015), but we note that we find a significantly different value for the extinction than these authors do. We find  $A_V \approx 1.0$  mag, whereas Fairlamb et al. (2015) find approximately zero extinction. Consequently, we derive a substantially larger stellar radius of  $R_\star \approx 3.9 R_\odot$ , compared to  $R_\star \approx 2.2 R_\odot$  found by Fairlamb et al. (2015); we find a correspondingly higher luminosity of  $L_\star \approx 24 L_\odot$ . Comparison to PMS evolutionary tracks yields a mass estimate of  $M_\star \approx 2.3 M_\odot$

<sup>10</sup> Available at

<https://www.stsci.edu/hst/instrumentation/reference-data-for-calibration-and-tools/astromonical-catalogs/calspec>.

and an age of  $\approx 3.4$  Myr, i.e. an object that is substantially more massive and younger than the  $\approx 1.6 M_{\odot}$  and  $\approx 8.1$  Myr found by Fairlamb et al. (2015). We note that a model with the parameters derived by Fairlamb et al. (2015), i.e. a 6500 K photosphere without appreciable foreground extinction, yields too blue a spectrum to be consistent with the observed optical photometry (see the grey curve in Fig. D.1).

Nowak et al. (2024) find a combined mass of  $\approx 2.3 M_{\odot}$  for the HD 142527 A & B system from a fit to the astrometrically measured orbit. Mass estimates for the companion range from  $\approx 0.13 - 0.34 M_{\odot}$  (Lacour et al. 2016; Christiaens et al. 2018), our total mass estimate is thus somewhat higher than that derived from the astrometric orbit.

## Appendix E: Dust opacity model

Table E.1: Parameters of the best-fit to the total  $N$ -band spectrum.

Parameter	Unit	Value
$\log(s/\text{sr})$		$17.18^{+0.07}_{-0.24}$
$w_{\text{PAH}}$		$1.28^{+1.31}_{-1.20}$
$T_c$	(K)	$420.98^{+23.36}_{-57.21}$
$w_{\text{cont}}$	(%)	$69.38^{+16.85}_{-3.65}$
$w_{\text{large, enst}}$	(%)	$2.54^{+53.41}_{-0.81}$
$w_{\text{small, enst}}$	(%)	$5.91^{+16.87}_{-5.56}$
$w_{\text{large, forst}}$	(%)	$2.10^{+19.92}_{-1.97}$
$w_{\text{small, forst}}$	(%)	$5.64^{+5.87}_{-5.50}$
$w_{\text{large, oliv}}$	(%)	$6.52^{+7.64}_{-6.52}$
$w_{\text{small, pyrox}}$	(%)	$1.37^{+8.13}_{-1.37}$
$w_{\text{large, unitl}}$	(%)	$7.73^{+3.44}_{-7.73}$
$w_{\text{small, unitl}}$	(%)	$1.70^{+1.42}_{-1.70}$
$\chi^2_{\text{r}}$		0.03

**Notes.** Parameters and uncertainties are determined as in Table 3. The  $\chi^2_{\text{r}} < 1$  presents the over-fitting caused by having one (averaged) data set with many degrees of freedom. The weights for the silicate stoichiometries (i.e. all weights excluding  $w_{\text{cont}}$  and  $w_{\text{PAH}}$ ) are normed to 100 %.

To analyse the composition of the prominent  $N$ -band silicate emission feature of HD 142527, we fit a model to the total  $N$ -band spectrum. The single-dish  $N$ -band spectroscopic data are comprised of the average of the spectra from the three MATISSE UT epochs. Adopting the methodology and dust components of van Boekel et al. (2005), we can describe the observed spectrum as a blackbody source function  $B_{\nu}(T)$  at a characteristic temperature  $T_c$  multiplied by a weighted sum of the opacities plus a polycyclic aromatic hydrocarbon (PAH) flux contribution:

$$F_{\nu, \text{model}} = (F_{\nu, \text{sil}} + F_{\nu, \text{cont}}) + w_{\text{PAH}} F_{\nu, \text{PAH}} = s B_{\nu}(T_c) \sum_k w_k \kappa_{\nu, \text{abs}, k} + w_{\text{PAH}} F_{\nu, \text{PAH}} \quad (\text{E.1})$$

The weights  $w$  for the dust stoichiometries, the weight  $w_{\text{PAH}}$  of the PAH, the characteristic temperature  $T_c$ , and the scale factor  $s$  are the free parameters of the fit.  $F_{\nu, \text{PAH}}$  is an empirical PAH spectral template adopted from van Boekel et al. (2005). There are

two weights for each dust stoichiometry, one for each grain size (i.e. 0.1 or 2  $\mu\text{m}$ ). The absorption opacities  $\kappa_{\nu, \text{abs}, k}$  are computed with the distribution of hollow spheres (DHS) (Min et al. 2005), using `optool`<sup>11</sup>, and Gaussian random field (GRF) (Min et al. 2007) methods, provided by M. Min. Their individual dust stoichiometries and structures are shown in Fig. E.1 and Table E.2.

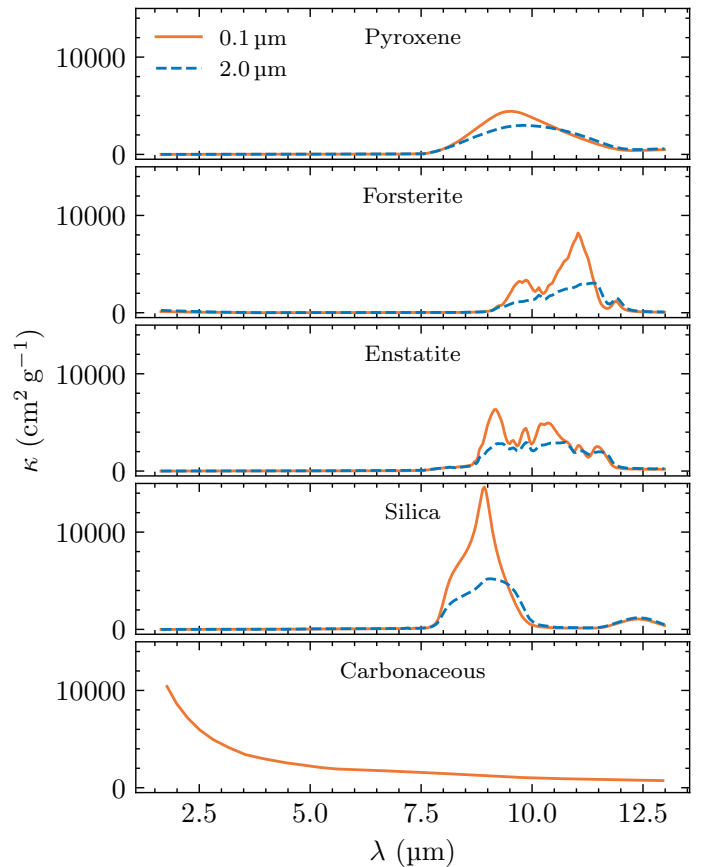


Fig. E.1: Mass absorption coefficients of the dust stoichiometries. Their type (amorphous or crystalline) and chemical formula are shown in Table E.2. The coefficients are used in modelling the opacity contributions of HD 142527 (Sect. 4.1).

For the continuum component, we chose amorphous carbonaceous grains as they are featureless in our wavelength range. We note that we do not directly constrain the nature of the continuum-emitting grains due to the lack of spectral features. Other species, such as iron, could also be used as an alternative to carbon.

Decoupling the opacities (Eq. 4) enables a unique silicate-to-carbonaceous ratio for the disc component (Sect. 4.2.2). This fit method yields a reasonable, albeit imperfect, approximation of the  $N$ -band (silicate) opacity (see Fig. 1). As we do not focus on quantitative dust spectroscopy, we replace the silicate feature of the best-fit model with that from the observed data via

$$\kappa_{\nu, \text{abs}, \text{sil}} = \frac{F_{\nu}}{s B_{\nu}(T_c)} - \kappa_{\nu, \text{abs}, \text{cont}}. \quad (\text{E.2})$$

<sup>11</sup>Available at <https://github.com/cdominik/optool>

Table E.2: Dust stoichiometries used in this work.

Stoichiometric (Grain) Type	Lattice Structure	Chemical Formula	Method	Grain Sizes	Reference
Pyroxene	Amorphous	$Mg_xFe_{1-x}SiO_3$	GRF	0.1, 2.0	(1)
Forsterite	Crystalline	$Mg_2SiO_4$	GRF	0.1, 2.0	(2)
Enstatite	Crystalline	$MgSiO_3$	GRF	0.1, 2.0	(3)
Silica	Crystalline	$SiO_2$	GRF	0.1, 2.0	(4)
Carbonaceous	Amorphous	C	DHS	0.1	(5)

**References.** (1) Dorschner et al. (1995); (2) Sogawa et al. (2006); (3) Jaeger et al. (1998); (4) Henning & Mutschke (1997); (5) Zubko et al. (1996);

**Notes.** Stoichiometries and sizes are inspired by previous analysis from van Boekel et al. (2005) and Juhász et al. (2010)

## Appendix F: Computation of observables

The complex correlated flux  $\mathfrak{F}_v$  is a linear operator, making it possible to sum up the complex correlated fluxes of individual components. From this sum, the total spectrum and the interferometric observables can then be extracted. First we have to de-project the observed spatial frequencies  $\mathbf{q} = (u, v) = (B_x/\lambda, B_y/\lambda)$  to reconstruct a face-on disc: following the steps from Berger & Segransan (2007) and Matter et al. (2014), we apply the counter-clockwise rotation matrix  $R(\theta)$  and the scaling matrix  $S(i)$  to de-project the spatial frequencies

$$\begin{aligned} q' = q'(i, \theta) &= \|S(i)R(\theta)\mathbf{q}\| \\ &= \left\| \begin{pmatrix} \cos(i) & 0 \\ 0 & 1 \end{pmatrix} \begin{pmatrix} \cos(\theta) & -\sin(\theta) \\ \sin(\theta) & \cos(\theta) \end{pmatrix} \begin{pmatrix} u \\ v \end{pmatrix} \right\|. \end{aligned} \quad (\text{F.1})$$

The de-projected spatial frequency  $q'(i, \theta)$  with its angle  $\psi = \arctan\left(\frac{u'}{v'}\right)$  is the polar coordinate representation of  $\mathbf{q}'$ .

With this, we can now compute the total spectrum, the correlated flux and the closure phase via the complex correlated flux as is shown in Buscher & Longair (2015): for the total spectrum, we take the real part of the complex correlated flux at its 0th spatial frequency and for the correlated fluxes, the modulus:

$$F_v = \Re[\mathfrak{F}_v(0)], \quad \text{and} \quad F_{v,\text{corr}} = |\mathfrak{F}_v|. \quad (\text{F.2})$$

The phase information is also contained in the complex correlated flux and can be extracted. However, due to the turbulence in the atmosphere, we cannot observe the absolute phases directly and make use of the closure phases instead:

$$\Phi_{\text{cp},ijk} = \phi_{ij} + \phi_{jk} + \phi_{ki}, \quad \text{with} \quad \Phi_{ij} = \phi_{ij} + \epsilon_i - \epsilon_j. \quad (\text{F.3})$$

Here,  $\phi_{ij}$  is the real phase between two telescopes, and  $\epsilon$  is the atmospheric aberration on a telescope. These atmospheric aberrations then cancel each other out in the closure triangle. To get the closure phase information, we compute the spatial frequencies of the closure triangles

$$\mathbf{q}_{ijk} = \begin{pmatrix} 1 & 0 \\ 0 & 1 \\ 1 & 1 \end{pmatrix} \begin{pmatrix} u_i & v_i \\ u_j & v_j \end{pmatrix}, \quad \text{where} \quad u_k = u_i + u_j. \quad (\text{F.4})$$

Then, we de-project the spatial frequencies via Eq. (F.1) and compute the closure phases via the bispectrum

$$\Phi_{\text{cp},ijk} = \arg(\mathfrak{F}_{ij}\mathfrak{F}_{jk}\mathfrak{F}_{ki}^*). \quad (\text{F.5})$$

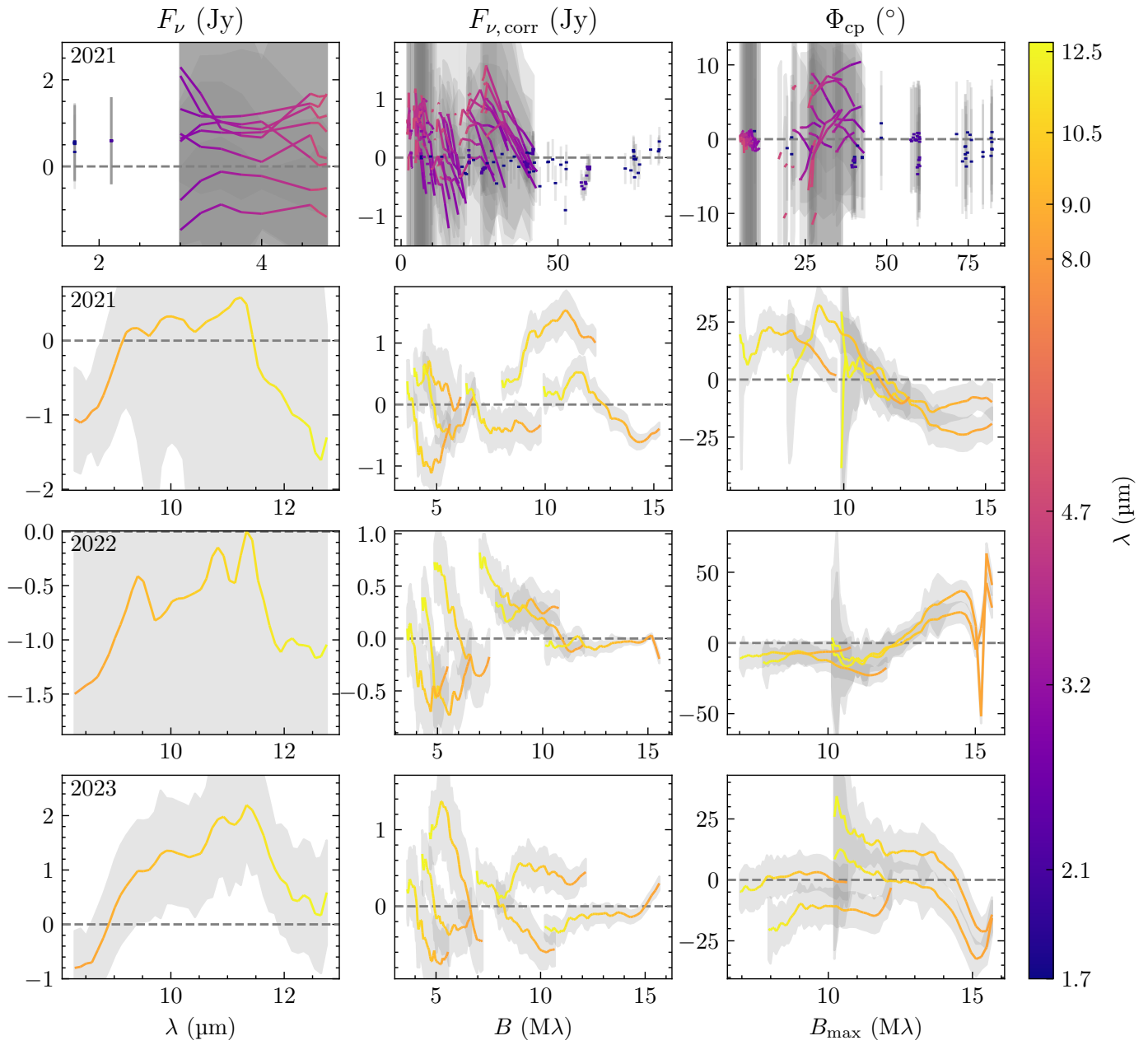


Fig. G.1: Residuals of Fig. 3 with identical layout.